

Discovery of Superconductivity and Electron-Phonon Drag in the Non-Centrosymmetric Semimetal LaRhGe₃

Mohamed Oudah,^{1,*} Hsiang-Hsi Kung,¹ Samikshya Sahu,^{1,2} Niclas Heinsdorf,^{1,2,3} Armin Schulz,³ Kai Philipp,³ Marta-Villa De Toro Sanchez,⁴ Yipeng Cai,⁴ Kenji Kojima,^{1,4} Andreas P. Schnyder,³ Hidenori Takagi,³ Bernhard Keimer,³ Doug A. Bonn,^{1,2} and Alannah M. Hallas^{1,2,5,†}

¹*Stewart Blusson Quantum Matter Institute, University of British Columbia, Vancouver, BC V6T 1Z4, Canada*

²*Department of Physics & Astronomy, University of British Columbia, Vancouver, BC V6T 1Z1, Canada*

³*Max Planck Institute for Solid State Research, Heisenbergstrasse 1, 70569 Stuttgart, Germany*

⁴*TRIUMF, Vancouver, British Columbia, V6T 2A3 Canada*

⁵*Canadian Institute for Advanced Research, Toronto, Ontario, Canada M5G 1M1*

(Dated: November 21, 2023)

We present a comprehensive study of the non-centrosymmetric semimetal LaRhGe₃. Our transport measurements reveal evidence for electron-hole compensation at low temperatures, resulting in a large magnetoresistance of 3000% at 1.8 K and 14 T. The carrier concentration is on the order of $10^{21}/\text{cm}^3$, higher than typical semimetals. We predict theoretically the existence of *almost movable* Weyl nodal lines that are protected by the tetragonal space group. We discover superconductivity for the first time in this compound with a T_c of 0.39(1) K and $B_c(0)$ of 2.1(1) mT, with evidence from specific heat and transverse-field muon spin relaxation (μSR). LaRhGe₃ is a weakly-coupled type-I superconductor, and we find no evidence for time-reversal symmetry breaking in our zero-field μSR . We study the electrical transport in the normal state and find an unusual $\sim T^3$ dependence at low temperature while Seebeck coefficient and thermal conductivity measurements reveal a peak in the same temperature range. We conclude that the transport properties of LaRhGe₃ in its normal state are strongly influenced by electron-phonon interactions. Furthermore, we examine the temperature dependent Raman spectra of LaRhGe₃ and find that the lifetime of the lowest energy A_1 phonon is dominated by phonon-electron scattering instead of anharmonic decay.

I. INTRODUCTION

Semimetals provide a fertile ground for investigating the interplay between topology, superconductivity, and electron-phonon interactions. Starting from the discovery of a Dirac semimetallic state in graphene [1, 2], the study of semimetals has grown to include ever more exotic flavors of topological states in materials with Dirac or Weyl crossings in their band structures [3–5]. Many topological semimetals are simultaneously found to exhibit remarkable transport properties including extremely large and non-saturating magnetoresistances and ultrahigh carrier mobilities [6–8]. In certain semimetals, these transport properties have been definitively linked with strong electron-phonon interactions, including WP₂ [9, 10], PtSn₄ [11, 12], and NbGe₂ [13, 14], all of which also manifest interesting topological states.

One particularly interesting class of semimetals are those with broken inversion symmetry. In metals, the breaking of inversion symmetry leads to symmetry allowed electronic and magnetic couplings that are forbidden in centrosymmetric materials, thereby promoting exotic states. One such example is antisymmetric spin-orbit coupling (SOC), which can significantly impact any superconducting state that arises. When the antisymmetric SOC is sufficiently strong, a mixture of

spin singlet and spin triplet pairings will occur yielding an unconventional superconducting state [15–19]. Similarly, asymmetric exchange in magnetic metals, namely the Dzyaloshinskii–Moriya interaction, can lead to complex magnetic states including chiral magnetic order [20] and skyrmion phases [21].

The rich physics associated with broken inversion symmetry has led to significant interest in the RTX_3 (R = rare earth, T = transition metal, X = Ge, Si, Sn) family of materials, which crystallize in the non-centrosymmetric $I4mm$ space group. Materials in this family have been known to exhibit heavy fermion behavior, complex magnetic states, and unconventional superconductivity [22–30]. In particular, they have attracted attention in light of their antisymmetric SOC split Fermi-surfaces [28]. It has been demonstrated in this class of materials that the transition element T plays a crucial role in the splitting of the Fermi-surface, while the R and X elements play a much smaller role [28].

Here, we report a comprehensive characterization of one member of the non-centrosymmetric RTX_3 family, LaRhGe₃, which has significant antisymmetric SOC due to the presence of Rh on the T site. We synthesize large single crystals of LaRhGe₃ using a self-flux method for the first time and characterize its low temperature electronic properties via transport, specific heat, muon spin relaxation, and Raman spectroscopy. This ensemble of measurements reveals a rich array of properties in LaRhGe₃ including semimetallicity, superconductivity, and electron-phonon drag. Our electronic structure calculations further reveal topological features of inter-

* Email: mohamed.oudah@ubc.ca

† Email: alannah.hallas@ubc.ca

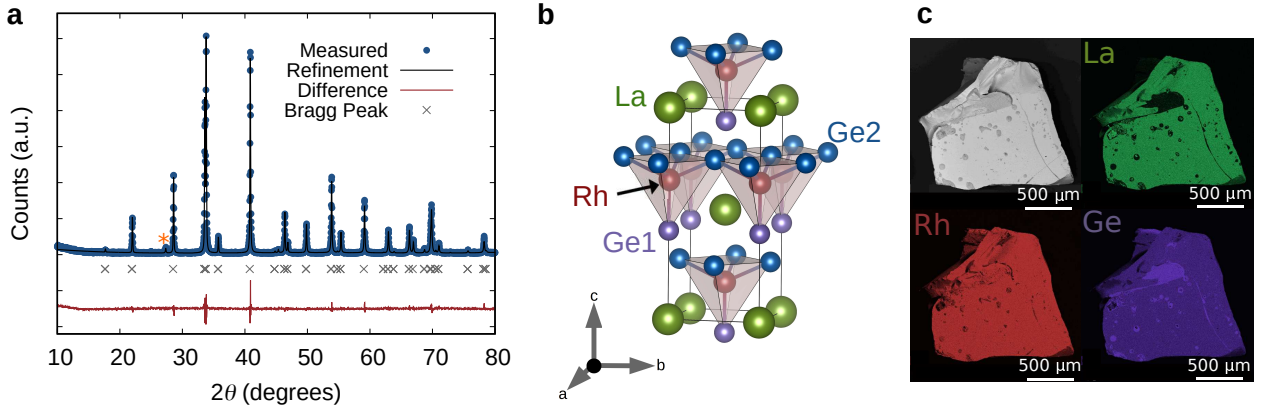


FIG. 1. Structural characterization of LaRhGe_3 . (a) Rietveld refinement of the powder X-ray diffraction pattern of LaRhGe_3 measured at room temperature. The Bragg peak positions for the $I4mm$ space group are indicated by the grey crosses. A small germanium metal impurity (1.3% by weight) peak is marked with an orange asterisk. (b) The non-centrosymmetric body-centered tetragonal crystal structure of LaRhGe_3 , where La is shown in green, Rh in red, and the two Ge sites are shown in purple and blue, respectively. The broken inversion symmetry is most easily appreciated by considering the positions of Rh within the unit cell. (c) Scanning electron microscopy image of a single crystal of LaRhGe_3 (top left) and elemental mapping on the same crystal for La (top right), Rh (bottom left), and Ge (bottom right). Intensity of colors in the elemental mapping corresponds to the intensity of peaks related to each element, showing uniform distribution of the elements across the crystal.

est, with the discovery of *almost movable* Weyl nodal lines. This unique set of results on LaRhGe_3 paves the way for further exploration of the $I4mm$ class of non-centrosymmetric materials.

II. RESULTS AND DISCUSSION

A. Non-Centrosymmetric Structure of LaRhGe_3

Large single crystals of LaRhGe_3 were grown by the metallic self-flux method. To confirm the structural characteristics and crystalline quality of our samples, we performed powder X-ray diffraction (XRD) and energy dispersive X-ray spectroscopy (EDX). The measured powder XRD pattern, given by the blue circles in Fig. 1(a), is consistent with the previously reported body-centered tetragonal $I4mm$ (no. 107) crystal structure [31]. Our Rietveld refinement, shown by the black line in Fig. 1(a), confirms the absence of any significant secondary phases. A minor germanium metal phase (1.3% by weight based on Rietveld refinement), likely originating from residual flux on the surface of the crystals, is marked by the orange asterisks. The fitted lattice parameters for LaRhGe_3 are $a = 4.4187(2)$ Å and $c = 10.0494(5)$ Å. The full results of the Rietveld refinement are presented in Tables S1 and S2.

The non-centrosymmetric crystal structure of LaRhGe_3 is presented in Fig. 1(b). The broken inversion symmetry can be easily discerned by considering the positions of Rh within the unit cell, where Rh sits at the center of the ab -plane with the lower half of the unit cell and at the unit cell edges in the upper half of the unit cell. There are two unique Ge sites in this structure,

with the Ge2 site having double the multiplicity of Ge1. The smallest interatomic distances in this structure are between Rh and Ge in a distorted corner-sharing square pyramidal configuration, where the single Rh-Ge1 distance is $2.377(3)$ Å and the four-fold Rh-Ge2 distance is $2.436(7)$ Å.

The spatial homogeneity of our crystals is confirmed by EDX mapping, which shows a uniform distribution of La, Rh and Ge on the sample surface (Fig. 1(c)). A ratio for La:Rh:Ge of 1.00:0.98:2.90 is found based on EDX analysis, which is close to the expected 1:1:3 ratio. Minor Ge-rich regions can be attributed to residual flux on the crystal's surface, as also detected in the powder XRD measurement.

B. Semimetallicity in LaRhGe_3

We begin our investigation of the electronic properties of LaRhGe_3 in its normal state. Electrical transport measurements confirm the metallic nature of this material, with a longitudinal resistivity that monotonically decreases with decreasing temperature and resistivity magnitudes in the $\mu\Omega\text{-cm}$ range across all temperature (Fig. 2(a)). The high residual resistivity ratio, $\rho_{300\text{K}}/\rho_{2\text{K}} = 110$, is suggestive of the good crystalline quality of our samples. As a function of increasing applied magnetic field, there is a rapid increase in the low temperature resistivity, below 50 K. For fields larger than 6 T, the resistivity reaches a minimum value before a low temperature upturn and then ultimately plateaus for temperatures below 10 K. In Fig. 2(b), we plot the magnetoresistance (MR) of LaRhGe_3 at various temperatures, where MR is defined as $[\rho_{xx}(B) - \rho_{xx}(0)]/\rho_{xx}(0)$. The MR remains unsaturated in fields

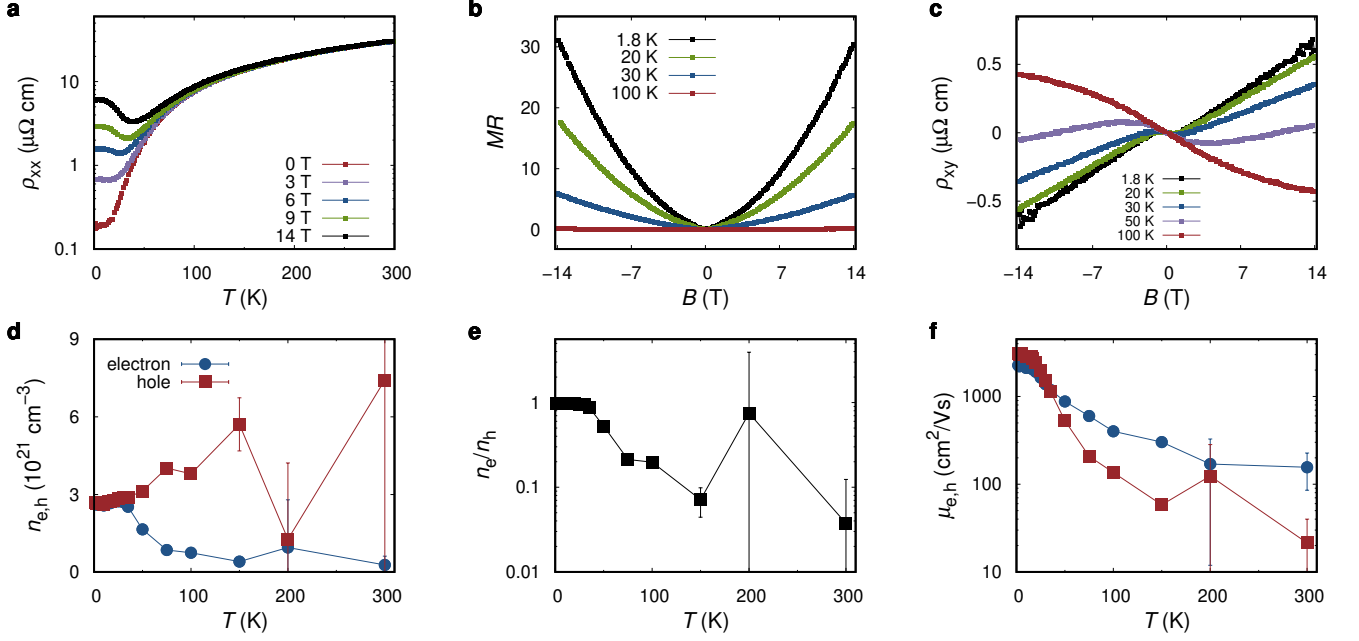


FIG. 2. Semimetallic electronic properties of LaRhGe₃. (a) Temperature dependence of the longitudinal resistivity ρ_{xx} measured in different magnetic fields, showing sizable magnetoresistance below 50 K. (b) Magnetic field dependence of the magnetoresistance (MR) as defined in text measured at various temperatures, reaching a value of 30 by 14 T at 1.8 K. (c) Hall resistivity ρ_{xy} measured at various temperatures, showing a change of sign upon cooling below 50 K. (d) Electron and hole carrier densities, (e) their ratio, and (f) carrier mobilities extracted from fits of MR and ρ_{xy} to a two-band model [32], revealing LaRhGe₃ to be a compensated semimetal at low temperatures.

up to 14 T, where it reaches a value of 30 at 1.8 K. The large and unsaturated MR and the field-driven resistivity upturn in LaRhGe₃ are characteristic of a compensated semimetal [33–35].

To verify the semimetallicity scenario, we measured the Hall resistivity ρ_{xy} of LaRhGe₃, shown in Fig. 2(c), at the same fields and temperatures as the MR. We find that $\rho_{xy}(B)$ is non-linear for all temperatures, and hence it cannot be fitted with a semi-classical one-band model for which ρ_{xx} would be independent of field, also in disagreement with our data. Instead, we fitted both the MR and Hall resistivity to a semi-classical two-band model [32]:

$$\rho_{xx} = \frac{1}{e} \frac{(n_h \mu_h + n_e \mu_e) + (n_h \mu_e + n_e \mu_h) \mu_h \mu_e B^2}{(n_h \mu_h + n_e \mu_e)^2 + (n_h - n_e)^2 \mu_h^2 \mu_e^2 B^2} \quad (1)$$

$$\rho_{xy} = \frac{B}{e} \frac{n_h \mu_h^2 - n_e \mu_e^2 + (n_h - n_e) \mu_h^2 \mu_e^2 B^2}{(n_h \mu_h + n_e \mu_e)^2 + (n_h - n_e)^2 \mu_h^2 \mu_e^2 B^2}. \quad (2)$$

The fitting parameters in this model are the carrier densities, n_e and n_h , and the carrier mobilities, μ_e and μ_h , for electrons and holes, respectively. We simultaneously fit ρ_{xx} and ρ_{xy} to this two-band model to extract $n_{e,h}$ and $\mu_{e,h}$ as a function of temperature. The carrier densities, plotted in Fig. 2(d), are on the order of 10^{21} cm^{-3} , as expected for a semimetal. At high temperature, we find that holes are the majority charge carriers but when

the temperature falls below 40 K, the carrier densities are essentially compensated with $n_e/n_h = 0.99(1)$ at 2 K, as can be seen in Fig. 2(e). For both holes and electrons, the mobility increases with decreasing temperature, as can be expected due to reduced scattering of charge carriers by phonons. At high temperature the electron mobility is larger than the hole mobility, as can be seen in Fig. 2(f). Upon cooling, the hole mobility increases more rapidly and exceeds the electron mobility for temperatures where the carriers are compensated, below 40 K, explaining the sign change observed in ρ_{xy} in the same temperature range. The high hole mobility of $0.3 \text{ m}^2/\text{Vs}$ at low temperature again demonstrates the good crystal quality, which is also relevant to the non-saturating MR of LaRhGe₃.

To further investigate the electronic properties of LaRhGe₃ we calculate its band structure using density functional theory (DFT). The band structure, which is plotted along the high symmetry directions of the body-centered tetragonal Brillouin zone (Fig. 3), is plotted according to each atomic site (La, Rh, Ge1, and Ge2), where the thickness and intensity of the color represent the weighted atomic contribution. Due to the presence of antisymmetric SOC, the spin degeneracy of all bands is lifted, as has been previously reported [28]. There are three pairs of spin-split bands crossing the Fermi level, where two pairs are hole bands and one pair is an electron band. All four atomic sites contribute to the bands closest to the Fermi level. The largest contribution to

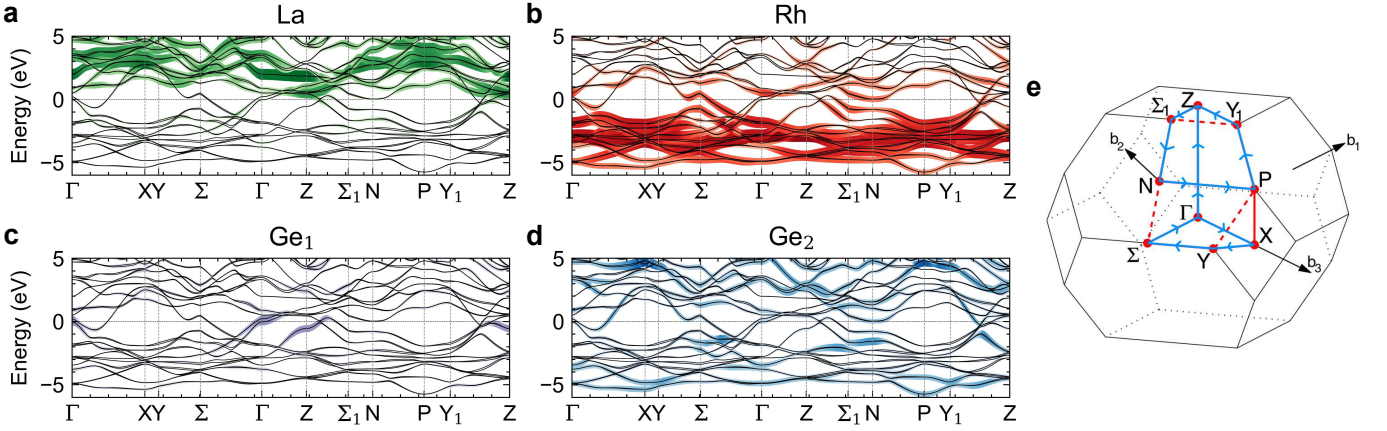


FIG. 3. *Ab-initio* electronic band structures in the primitive unit cell of LaRhGe_3 . The width and intensity of the superimposed colors indicate the contribution to the states from the respective atoms. The red horizontal line marks the Fermi level. An onsite Hubbard interaction of $U_{LDA+U} = 14.5$ eV was added to the f -orbitals of La to push the (unoccupied) states out of the energy window.

all the bands that cross the Fermi energy originates from Rh, while Ge1 contributes to the hole bands, and Ge2 contributes to the electron bands. We note that our extracted de Haas-van Alphen (dHvA) oscillation frequencies, as shown in Supplemental Fig. S1, are consistent with previous studies and the calculated band structure. There are three pairs of bands, one electron and two hole, crossing the Fermi level, where the pairs are split in energy due to the antisymmetric SOC [28].

C. Protected Nodal Lines in LaRhGe_3

Next we highlight aspects of symmetry-enforced band crossings in LaRhGe_3 . Group theoretical analysis recently predicted *almost movable nodal lines* in a number of tetragonal space groups including the $I4mm$ group to which LaRhGe_3 belongs [36]. Their specific dispersion relation and proximity to the Fermi level, as well as their connectivity is not fully fixed by symmetry alone, and in general depends on the particular material. In the case of LaRhGe_3 , even though the global Kramers' degeneracy is lifted, the $I4mm$ space group symmetry enforces two types of two-fold degenerate nodal lines throughout the Brillouin zone. Consider the mirror plane that intersects the rotational axis (Γ - Z) and the N -point. The eigenvalues of the mirror symmetry at N are $\pm i$. Because N is a time reversal invariant momentum (TRIM) point, the $+i$ and $-i$ eigenvalues are paired, enforcing a two-fold degeneracy at this point. Let \mathbf{k}_1 and \mathbf{k}_2 be two k -points on the mirror plane that are related by time reversal. Because they are time reversal partners, their mirror eigenvalues have opposite phase. Therefore, along an arbitrary path on the mirror plane that connects \mathbf{k}_1 and \mathbf{k}_2 (which does not cross a TRIM point), the eigenvalues must be exchanged. Since this can only happen at band crossings and we have the freedom to choose any

path, the intersections must form a nodal line that connects the N -points. That type of degeneracy is called an *almost movable* nodal line [36]. It is only pinned at the two TRIMs that it connects, and in contrast to a point-like topological band feature (*e.g.* a Weyl point) it is extended in both k -space and energy. The same argument holds for the Γ - and Z -point. However, the presence of additional symmetry pins the nodal line to the rotational axis. Hence, there are two ways the almost movable nodal line can connect the N -points: It either intersects the pinned nodal line (Γ - Z) or it does not.

In Figure 4(a) and 4(b) the two types of connectivity are shown. The intensity of the heatmap corresponds to a quantity similar to a spectral function that has poles at k -points where a chosen pair of bands becomes degenerate. The overlay shows the body-centered primitive Brillouin zone (type 2) and the high-symmetry points that lie within the plane spanned by Γ - Z and Γ - N . The almost movable nodal lines connect the N -points on (seemingly arbitrary) paths that depend on the specific dispersion relation of the chosen pair of bands. Thus, the evolution of the almost movable nodal lines through k -space for different band pairs varies drastically. Figure 4(c) shows the dispersion relation along the different nodal lines. The pinned and the almost movable nodal lines shown in panel (a) are close to the Fermi energy and can potentially be tuned to the Fermi edge by either doping or applying a gate voltage. Due to the dispersive nature of the nodal lines, there is a large energy region in which the degeneracies can be accessed in contrast to point-like topological band crossing, and thus a wider range of parameters in which drumhead surface states can be found [37, 38]. Even though surface states do not necessarily emerge in nodal line systems [39], any curve through k -space that encircles a single nodal line has a Berry curvature that is quantized to π by the mirror sym-

metry. It is very likely that a suitable surface termination can be found, for which gapless surface states appear at k -points of the two-dimensional surface Brillouin zone that connect projections of the different nodal lines in the bulk. Materials with these gapless and robust surface modes are highly sought-after, due to the variety of proposals in novel device applications [3, 40–46]. In realistic materials, disorder and defects weakly break the crystal symmetries that protect both the nodal lines and their edge modes. However, as long as the symmetries are approximate and the effect of the perturbation is small compared to the topological gap, the edge modes remain present [47, 48]. Interaction effects might also weakly break symmetries, but more importantly they generically obstruct an exact description of a material’s electronic structure using single-particle states, which the definition of most topological invariants relies on. Nevertheless, it has been shown that an interacting system can always be adiabatically connected to a noninteracting system with the same topology, as long as the interaction does not drive a phase transition [49–52]. Even nonlinear perturbations do not generically suppress edge modes [53], and their stability in nodal line semimetals in their superconducting state has been theoretically demonstrated [54].

Exploring the evolution of these *almost movable nodal lines* in other materials with the $I4mm$ space group but different elements should be the subject of future studies. Our calculations have established the compensated semimetal state in LaRhGe_3 with an antisymmetric SOC-split Fermi surface and *almost movable nodal lines*; we next highlight our discovery of superconductivity in LaRhGe_3 .

D. Superconductivity in LaRhGe_3

As our electrical transport measurements do not extend to sufficiently low temperature, our first indication of superconductivity in LaRhGe_3 came from low temperature specific heat measurements, as shown in Figure 5(a), where a sharp anomaly is observed at $T_c = 0.39(1)\text{ K}$. Upon application of small magnetic fields, the transition is suppressed to lower temperatures. We find that the transition remains sharp for applied fields of 0.5 mT and 1 mT, despite the decrease in T_c , which is consistent with a first order transition as expected for a type-I superconductor. Upon application of a 2 mT field the superconducting transition is fully suppressed in our measurement window, which extends down to 0.1 K.

To further investigate the superconducting state of LaRhGe_3 , we performed muon spin relaxation (μSR) measurements. The muon decay asymmetry plotted as a function of time in an applied transverse field (TF) of 1 mT (which is below the critical field) is shown in Fig. 5(b). The field was applied perpendicular to the plate-like crystals and the muon spin is parallel to the plate of the crystal, such that the muon spin is perpendicular to the field applied. The muons precess in the ap-

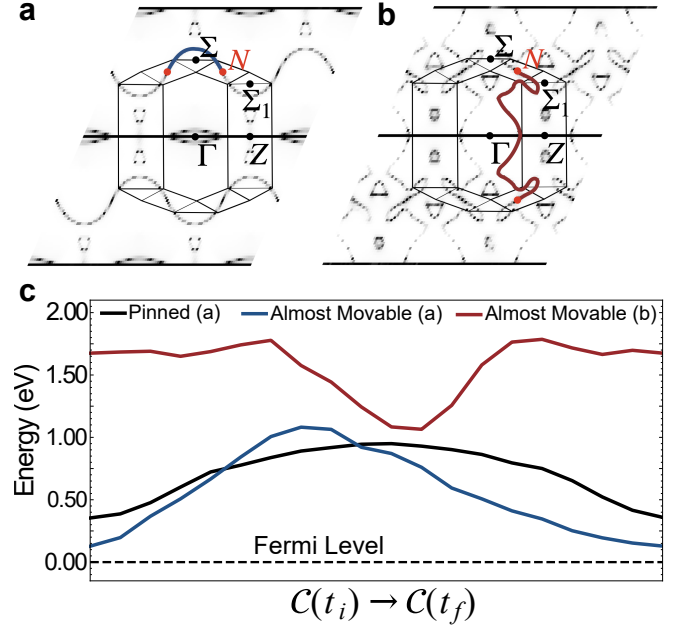


FIG. 4. Almost movable nodal lines in LaRhGe_3 . (a,b) Pinned (Γ to Z , black) and almost movable nodal lines (N to N , (a) blue and (b) red) in the mirror plane of the Brillouin zone of the type 2 body centered tetragonal primitive unit cell. The projection of the Brillouin zone onto this mirror plane, as well as the high-symmetry points that lie therein are given in the overlay. The connectivity of almost movable nodal lines is not completely determined by the space group symmetry. The two possibilities are both realized in the material for different pairs of bands. (a) Almost movable nodal line connecting two N -points. (b) Same as (a), but intersecting the pinned nodal line. (c) The dispersion along curves C through k -space along the pinned nodal line from (a) (black), the almost movable nodal line from (a) (blue) and the almost movable nodal line from (b) (red). t parameterizes the curve with $C(t_i)$ and $C(t_f)$ being the initial and final point of the curves respectively. The pinned and the almost movable lines from (a) are close to the Fermi level.

plied field, yielding an oscillating decay asymmetry. The measurement above T_c is shown in red while the measurements below T_c under zero-field cooled (ZFC) and field cooled (FC) conditions are shown in blue and green, respectively. We observe an increase in relaxation below T_c under both the field-cooled and the zero-field-cooled conditions, which results in a smaller amplitude of the oscillations. We fit the asymmetry spectra using a two term sinusoidal decaying function

$$G_{\text{TF}}(t) = A \left[f \exp\left(\frac{-\sigma^2 t^2}{2}\right) \cos(\omega_1 t + \phi) + (1 - f) \exp(-\lambda t) \cos(\omega_2 t + \phi) \right]$$

where the first term captures the signal from muons stopping in the sample and the second term captures the signal from muons stopping in the silver sample holder. The fraction of signal from muons that land in the sample is given by f , while ω_1 and ω_2 are the muon precession fre-

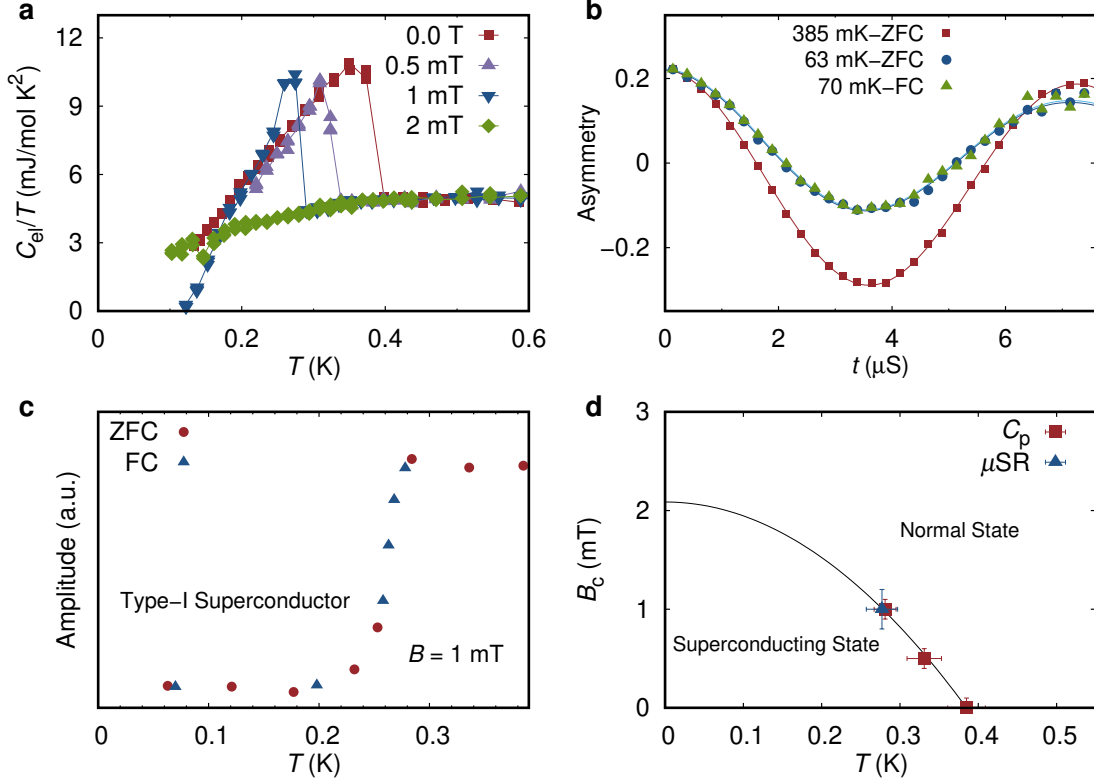


FIG. 5. Superconducting transition in LaRhGe₃. (a) Temperature dependence of C_{el}/T measured in varying magnetic fields. The superconducting transition seen at 0.39(1) K in 0 mT is suppressed with increasing magnetic field. (b) Representative transverse field muon decay asymmetry spectra collected above and below T_c in LaRhGe₃ under an applied magnetic field of 1.0 mT. (c) The amplitude of the signal in (b) as a function of temperature measured in zero-field cooling (ZFC) and field cooling (FC) protocol. Reduction in amplitude is due to expulsion of magnetic field in the superconducting state, and the ZFC and FC show similar suppression, demonstrating type-I superconductivity. (d) Field dependence of the T_c values extracted from C_p and transverse field μ SR. The solid line is a fit to the data used to estimate $B_c(0) = 2.1$ mT.

quencies in the sample and the background, respectively. The A term is the total asymmetry and the ϕ is the initial phase of the muons. The depolarization rates for the sample and the background signals, respectively, are given by σ and λ .

The fitted amplitude of the oscillating component as a function of temperature under both ZFC and FC conditions is shown in Fig. 5(c). The amplitude corresponds to all muons stopping inside the superconducting LaRhGe₃ and the non-superconducting silver plate. A sharp drop in amplitude is observed at the superconducting transition. This behavior is expected in a superconductor due to the expulsion of magnetic field from the bulk of the sample in the superconducting state such that muons implanted sufficiently deeply in the sample will not feel the applied field and will therefore not precess. From these transverse field μ SR measurements, we estimate $T_c \sim 0.28$ K in an applied field of 1 mT, in good agreement with the T_c measured in specific heat at 1 mT. We find that the suppression of the amplitude is approximately equivalent under ZFC and FC conditions at the lowest temperatures, which indicates that LaRhGe₃ is a Type-I superconductor. The temperature and field dependence

of T_c extracted from specific heat and transverse field μ SR are plotted in Fig. 5(d).

To further characterize the superconductivity of LaRhGe₃, we next turn to modelling its specific heat. Above $T_c = 0.39(1)$ K the C_p data are well described by

$$C_p = \gamma_n T + \beta T^3 \quad (3)$$

where fitting the data yields the Sommerfeld coefficient $\gamma_n = 4.92(4)$ mJ mol⁻¹ K⁻² and $\beta = 0.25(1)$ mJ mol⁻¹ K⁻⁴. The phonon contribution is represented by the cubic term βT^3 and the Debye temperature Θ_D is then calculated according to

$$\Theta_D = \left(\frac{12\pi^4}{5\beta} n R \right)^{1/3} \quad (4)$$

where n , the number of atoms per formula unit, is 5 and R is the gas constant 8.314 J mol⁻¹ K⁻¹, giving $\Theta_D = 341(10)$ K. Next, taking Θ_D and T_c , we calculate the superconducting parameter λ_{ep} using the inverted McMillan [55] equation

$$\lambda_{ep} = \frac{1.04 + \mu^* \ln \left(\frac{\Theta_D}{1.45 T_c} \right)}{(1 - 0.62 \mu^*) \ln \left(\frac{\Theta_D}{1.45 T_c} \right) - 1.04} \quad (5)$$

where $\mu^* = 0.10$ and $T_c = 0.39(1)$ K. We find $\lambda_{ep} = 0.34(2)$ for LaRhGe₃, suggesting it is a weak coupling superconductor. Using λ_{ep} , γ , and the Boltzmann constant k_B , we calculate the electronic density of states (DOS) at the Fermi energy $N(E_F)$ with the equation

$$N(E_F) = \frac{3\gamma}{\pi^2 k_B^2 (1 + \lambda_{ep})} \quad (6)$$

$N(E_F)$ was estimated to be 1.56 states eV⁻¹ per formula unit of LaRhGe₃. From our DFT calculations we find the DOS at the Fermi energy $N(E_F)^{calc}$ of 3.24 states eV⁻¹ per formula unit, and we evaluate the effective mass based on specific heat to be $m^*/m_e = N(E_F)/N(E_F)^{calc} = 0.54$. This reduced effective mass compared with the free electron mass is consistent with LaRhGe₃ being a semimetal, and the value of $m^*/m_e = 0.54$ falls within the cyclotron effective masses, $m^*/m_e \sim 0.23$ -1.04, reported previously by Kawai *et al.* [28].

The applied magnetic fields plotted against T_c as extracted from C_P measurements and transverse-field μ SR are shown in Fig. 5(d). We estimate the zero-temperature critical field $B_c(0)$ using the conventional relationship below

$$B_c(T) = B_c(0) \left[1 - \left(\frac{T}{T_c} \right)^2 \right] \quad (7)$$

where T_c is 0.39(1) K we obtain the curve in red to the data extracted from C_P . This fit yields a $B_c(0)$ of 2.1 mT. We have been unsuccessful so far in measuring the drop in resistivity to zero below T_c , which is most likely due to the low critical current of LaRhGe₃, consistent with its low critical field. Our current capabilities for measuring resistivity with the dilution fridge do not allow us to apply a low enough current to perform the measurement. The small critical field makes the presence of a small remnant field during the C_P measurement a serious concern that can shift our measured T_c . However, to address this concern we highlight the point on this phase diagram extracted from transverse field μ SR measurement, where magnetic field for this point is extracted from the fit to transverse field μ SR experiment, which is expected to be accurate and confirms the fit of $B_c(0)$ based on the C_P data.

The magnitude of the specific heat jump $\Delta C/C_{en} \sim 1.43$, C_{en} being the electronic specific heat in the normal state, is consistent with that expected for a BCS model in the weak-coupling limit. The BCS model, shown in black in Fig. 3(a), fits the data well just below T_c , but

TABLE I. Superconducting parameters of LaRhGe₃.

| Parameter | Value | Units |
|----------------|---------|--------------------------------------|
| T_c | 0.39(1) | K |
| $B_c(0)$ | 2.1(1) | mT |
| γ_n | 4.92(4) | mJ mol ⁻¹ K ⁻² |
| β | 0.25(1) | mJ mol ⁻¹ K ⁻⁴ |
| θ_D | 341(10) | K |
| λ_{ep} | 0.34(2) | - |

some deviations appears at lower temperatures. With the current C_P we cannot conclude whether the gap structure of LaRhGe₃ is an isotropic *s*-wave gap or whether the gap structure has some nodes, and this will be the subject of future experiments going to lower temperatures.

To check whether the superconductivity in LaRhGe₃ breaks TRS we perform muon measurements in zero-field, since muons are a sensitive probe to magnetic fields in the sample. We check for any spontaneous magnetic fields inside the superconducting state by performing the measurement above and below T_c , as shown in Fig 6(c). In the absence of magnetism, the muon depolarization is due to randomly oriented nuclear moments, and can be described with Kubo-Toyabe function below

$$G_{KT}(t) = \frac{1}{3} + \frac{2}{3} (1 - \sigma^2 t^2) \exp \left(-\frac{\sigma^2 t^2}{2} \right)$$

where σ accounts for the field generated by the randomly nuclear moments at the muon site. The relaxation spectra for LaRhGe₃ is fitted to the function

$$A(t) = A_S G_{KT}(t) \exp(-\Lambda t) + A_{BG}$$

where A_S , A_{BG} represent the sample and background asymmetry, respectively, and the Λ accounts for any additional relaxation rate. By fitting the data to the equation above, we find no significant change in Λ above and below T_c ; the results of the fitted value are shown in the inset of Fig. 6(c). This indicates the absence of any significant TRS breaking in LaRhGe₃.

While pure elements tend to host type-I superconductivity rather than type-II, most compound superconductors are type-II. Only a few binary compounds exhibit type-I superconductivity, and even fewer ternary compounds. LaRhGe₃ is one of very few type-I superconductors containing more than two elements. Other ternary type-I superconductors include LaPd₂Ge₂ [76], (Y, La, Lu)Pd₂Si₂ [77], LaRh₂Si₂ [77], Ag₅Pb₂O₆ [78], and LaRhSi₃ [70]. We compare the T_c , γ_n , and $B_c(0)$ values for various superconductors in the *I4mm* space group, including LaRhGe₃ and LaRhSi₃. Despite the comparable γ_n values for all of these materials, we have varying superconducting T_c and critical fields. Whether this difference is due to details of electronic band structure or atomic size effects is unclear at the moment, but should be further investigated in future studies.

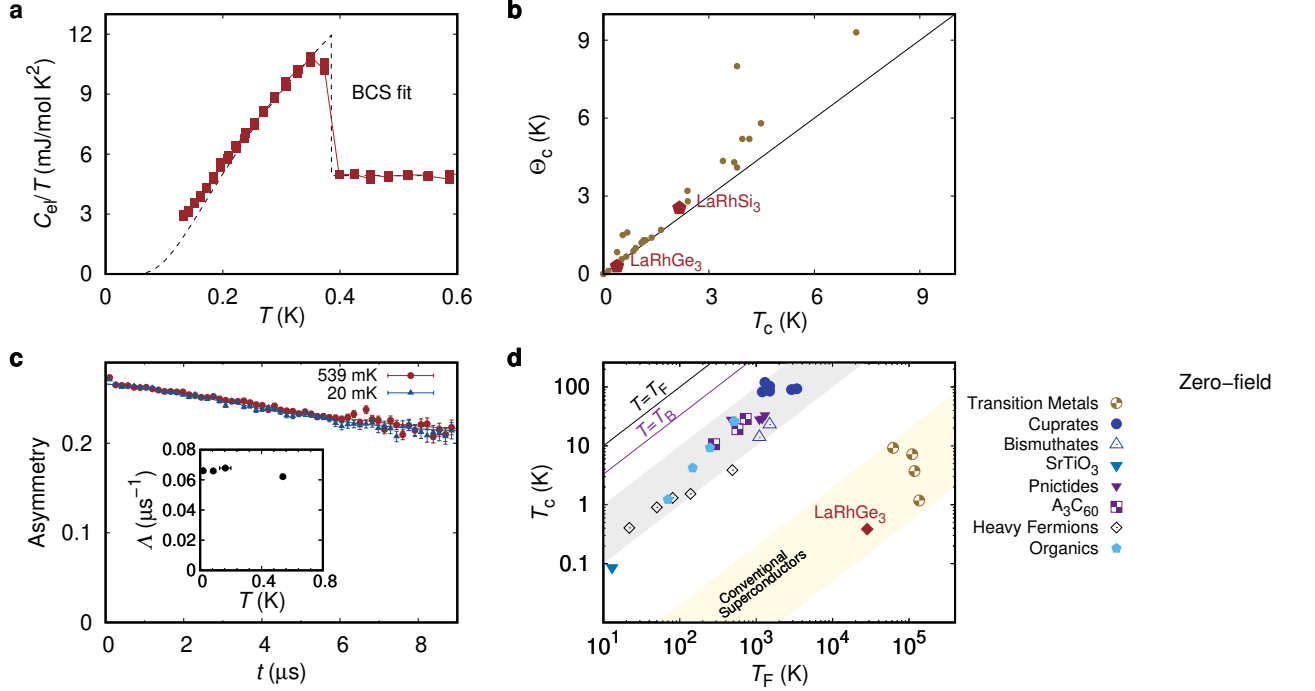


FIG. 6. Type-I BCS nature of the superconducting state in LaRhGe₃. (a) Superconducting transition of LaRhGe₃ in the electronic part of the specific heat C_{el}/T as a function of T in 0 T. The dashed black line is a fit for a T_c of 0.39(1) K for weak-coupling BCS behavior. (b) Plot of Θ_c against measured T_c for various elemental type-I superconductors, LaRhSi₃, and LaRhGe₃. LaRhGe₃ falls on the black solid line, which represents the expectation based on weak-coupling BCS theory. (c) Zero field μ SR spectra collected at 539 mK and 20 mK, with fit using Kubo-Toyabe function for the data. No significant change is seen between the data above and below T_c . Inset shows the resulting relaxation rate σ . (d) Uemura plot showing the superconducting transition temperature (T_c) vs the Fermi temperature (T_F) for various superconductors [56–67], where LaRhGe₃ falls within the region of conventional superconductors. $T = T_B$ line in purple represents the Bose-Einstein condensation temperature of an ideal three-dimensional boson gas, and $T = T_F$ line is shown in black.

TABLE II. Superconductivity in LaRhGe₃ compared with other superconductors in $I4mm$ space group.

| Compound | T_c (K) | γ_n (mJ mol ⁻¹ K ⁻²) | $B_{c2}(0)$ (T) | Reference |
|--------------------------------|-----------|----------------------------------------------------|------------------|-------------|
| Ba(Pt,Pd)Si ₃ | 2.3–2.8 | 4.9–5.7 | 0.05–0.10 | [68, 69] |
| La(Rh,Pt Pd,Ir)Si ₃ | 0.7–2.7 | 4.4–6 | Type I/0.053 | [24, 70–73] |
| Ca(Pt,Ir)Si ₃ | 2.3–3.6 | 4.0–5.8 | 0.15–0.27 | [29, 74] |
| Sr(Ni,Pd,Pt)Si ₃ | 1.0–3.0 | 3.9–5.3 | 0.039–0.174 | [69] |
| Sr(Pd,Pt)Ge ₃ | 1.0–1.5 | 4.0–5.0 | 0.03–0.05 | [69, 75] |
| LaRhGe ₃ | 0.39(1) | 4.92(4) | Type I/0.0021(1) | This work |

In Fig. 6(b), we compare the expected critical temperature denoted as θ_c based on the γ_n and T_c values with the following equation [79]:

$$\Theta_c = \frac{2B_c(0)}{\sqrt{1.43\mu_0\gamma_n}} \quad (8)$$

with the measured T_c for various elemental type-I superconductors, LaRhSi₃ [70], and LaRhGe₃. We find that LaRhGe₃, as well as LaRhSi₃ [70], lie close to the solid-black line that represents the expectation based on weak-coupling BCS. This is consistent with our analysis of the

jump in C_P and further confirms that LaRhGe₃ is a type-I superconductor in the weak-coupling limit. LaRhGe₃ and LaRhSi₃ have similar degrees of antisymmetric SOC [25, 80], and we find no sign of unconventional superconductivity in the silicide [70] nor in our bulk measurements on LaRhGe₃.

We evaluate the Fermi temperature T_F for a 3D system via the relation $T_F = (\hbar^2/2)(3\pi^2)^{2/3}n^{2/3}/k_B m^*$ [56], where n is the density of quasiparticles per unit volume. We use the low temperature carrier density from our Hall measurements and the effective mass estimated from specific heat to obtain $T_F = 28340$ K and $T_c/T_F =$

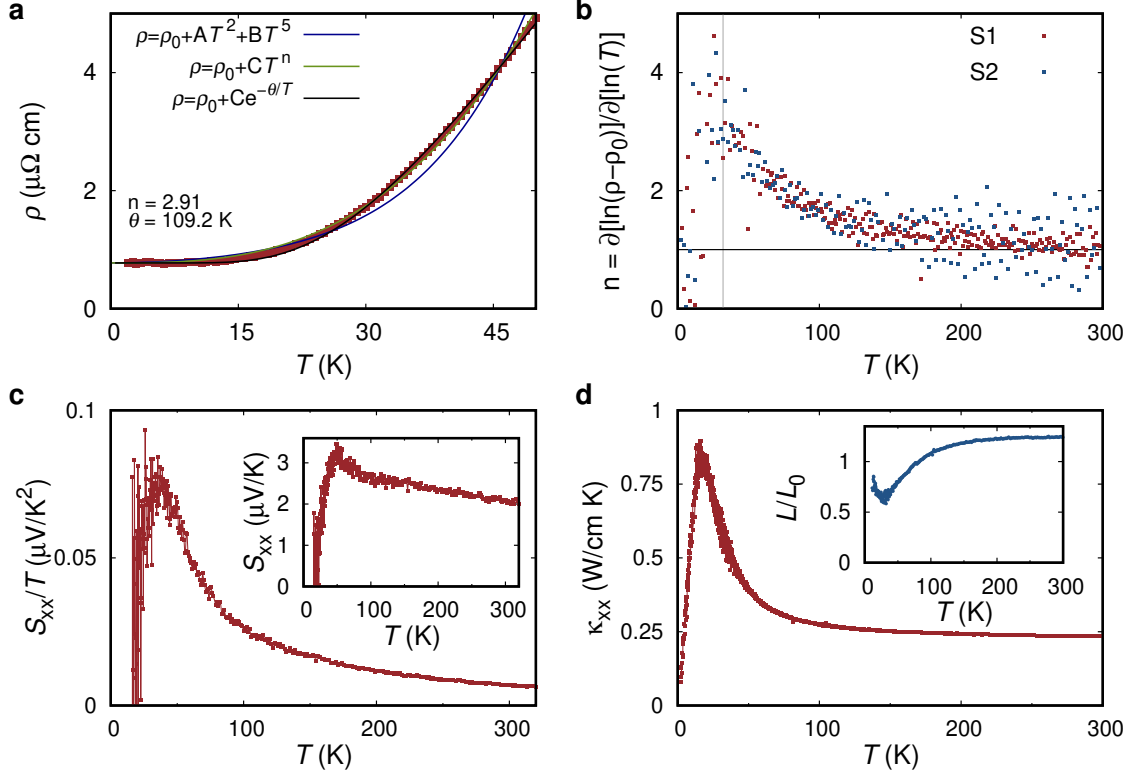


FIG. 7. Electron-phonon drag in LaRhGe₃. (a) Resistivity as a function of temperature measured along *ab*-plane of LaRhGe₃ in zero-field, and different models fitted to the data below 50 K. (b) n , the exponent of the temperature dependent resistivity determined derivative of $\ln(\rho - \rho_0)$ vs. $\ln(T)$ as a function of temperature. Data for two samples, S1 and S2, are shown. (c) Temperature dependence of Seebeck coefficient over temperature (S_{xx}/T as a function of temperature of LaRhGe₃. Inset shows S_{xx} as a function of temperature. (d) Temperature dependence of thermal conductivity of LaRhGe₃. Inset shows the Lorentz number as a function of temperature.

1.36×10^{-5} , which places LaRhGe₃ in a region with other conventional superconductors. This further confirms that the ternary compound LaRhGe₃ can be described in the bulk as a BCS superconductor in the weak-coupling limit. Next we highlight electron-phonon interactions in the normal state of LaRhGe₃.

E. Electron-Phonon Drag in LaRhGe₃

Finally, we return to the normal state of LaRhGe₃ to investigate the thermal properties of this material. Our first indication of unusual transport behavior came from zero-field resistivity where we observe a deviation from a standard Fermi liquid behaviour as shown in Fig. 7(a). Using the typical $\rho = \rho_0 + AT^2 + BT^5$ to account for electron-electron interactions with the T^2 term and electron-phonon interactions with the T^5 term fits the data poorly below 50 K, and the extracted coefficients $A = 6.24 \times 10^{-4} \mu\Omega\text{cm K}^{-2}$ and $B = 1.425 \times 10^{-8} \mu\Omega\text{cm K}^{-5}$ are physically unreasonable. If we use the A -coefficient along with the Sommerfeld coefficient from specific heat we evaluate a Kadowaki-Woods ratio of $R_{KW} = \frac{A}{\gamma^2} = 12.4 \mu\Omega\text{cm mol}^2\text{K}^2\text{J}^{-2}$, which is compa-

rable with heavy fermions. However, we have no evidence of heavy Fermion behaviour in LaRhGe₃ considering the absence of *f*-electrons and the low effective mass established from dHvA measurements [28]. Instead, we find that the resistivity data fits well to a phonon-drag model $\rho = \rho_0 + Ce^{-\theta/T}$. The exponential fit yields $\theta = 110\text{ K}$, which is approximately one-third of the Debye temperature of $\theta_D \sim 341\text{ K}$ determined from specific heat measurements. Also, we find an equally good agreement the data with a power law fit $\rho = \rho_0 + T^n$, which yields $n = 2.9$. A value of $n = 3$ can arise due to selective phonon mode softening associated with electron-phonon drag in materials [81].

Furthermore, to analyze the temperature dependence of the resistivity we take the logarithmic derivative after subtracting residual resistivity to quantify the exponent $n = [\delta \ln(\rho - \rho_0)] / [\delta \ln T]$. This analysis has been applied to extract the exponent in antimony, heavy fermions, cuprates, and strontium titanate [82]. The temperature dependence of n is presented in Fig. 7(b) for two different samples, and we find at high temperature $n \sim 1$ as expected in a standard Bloch-Grüneisen picture. However, we find an upturn towards $n \sim 3$ at low temperature, which is consistent with $n = 2.9$ from our power law

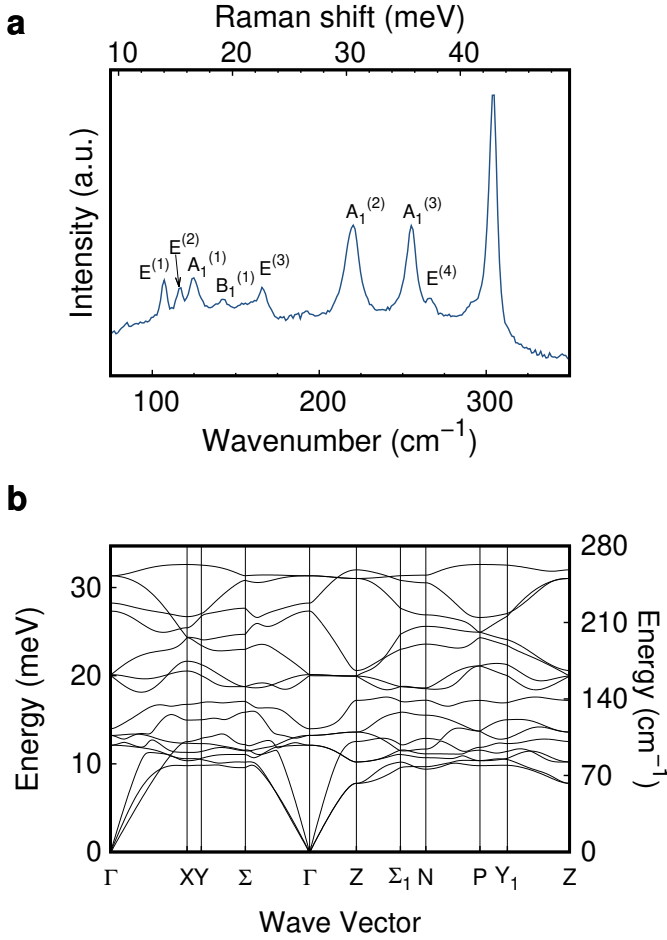


FIG. 8. Phonon spectrum of LaRhGe₃. (a) Raman spectra of LaRhGe₃ measured at 10 K. The phonon mode symmetries are labelled in accordance with our DFT calculations. The strong peak at 300 cm⁻¹ is likely due to Ge flux on the surface. (b) Calculated phonon dispersion curves along high-symmetry lines of the tetragonal primitive unit cell of LaRhGe₃

fit above. The lowest temperature data is too noisy to identify any n value.

To further explore the phonon-drag scenario, we measure the Seebeck coefficient at low temperature, shown in Fig. 7(c), and notice a peak at around ~ 50 K signaling the interaction between phonons and electrons is enhanced at low temperature. The Seebeck coefficient over temperature, inset of Fig. 7(c), pushes the peak to an even lower temperature of ~ 30 K similar to the peak in the derivative of the resistivity. A peak below 50 K in the thermal conductivity, shown in Fig. 7(d), provides another proof for the electron-phonon drag scenario. Typically, the Lorentz number is evaluated by dividing the electronic part of the thermal conductivity by the electrical conductivity, but separating the phonon and electron parts of the thermal conductivity proved difficult with our current data. Instead, we show the total thermal conductivity divided by electrical conductivity, representing

an upper limit of the Lorentz number, in the inset of Fig. 7(d), which shows clear deviation at low temperature with a minimum at around 30 K. A Kohler plot can be utilized to scale the MR over the various temperatures measured, and in our current measurements we find no clear change around 30 K as shown in the supplemental materials Fig. S5.

We measure the C_P up to 300 K, shown in Fig. S6(c), and confirm consistency with the Dulong-Petit limit at high temperature and find no anomalies at low temperature. The Debye temperature of 341 K estimated in Sec. IID is consistent with our high temperature data. The peaks in κ , S , and derivative of the resistivity appear at ~ 30 K, which represent a phonon-drag temperature. Comparing this with the Debye temperature or 340 K, we find $\Theta_{\text{ph-drag}}/\Theta_D \sim 10$, which has been seen in other materials with phonon-drag. We notice in the MR data that a significant enhancement appears at around 30 K that we attribute in Sec. IIB to electron-hole compensation, but the connection with electron-phonon interactions is unclear at the moment and should be the subject of future studies.

To confirm the electron-phonon drag model, we measure the Raman spectra between 300 and 10 K to search for signatures of phonon line width broadening due to electron-phonon coupling, previously observed in some conventional superconductors [83, 84], and more recently reported in WP₂ and NbGe₂ [10, 13]. Due to the lack of inversion symmetry, all 12 optical phonons are Raman active in LaRhGe₃, which we will denote by the irreducible representations of the C_{4v} point group: $3A_1 + B_1 + 4E$ [85]. Using the Raman selection rules and polarization optics [86], we identify the peaks at 121, 214, and 249 cm⁻¹ as the 3 A_1 phonons, the peak at 139 cm⁻¹ is a B_1 phonon, whereas the peaks at 106, 116, 163, and 262 cm⁻¹ are the phonons with E symmetry (Fig. S2). The Raman spectrum measured at 10 K without any analyzing polarizer is shown in Fig. 8(a) with all phonon modes labeled. We tabulate the measured phonon energies along side the values calculated from DFT in Table S4 to justify our mode assignment. We also notice that there are two unaccounted peaks at 153 and 189 cm⁻¹, which we designate as phonon overtones, i.e. the simultaneous excitation of two phonons carrying opposite momenta. Our assignment is justified by the DFT calculated phonon dispersion, where the acoustic phonon branch has maximum energy around 80-90 cm⁻¹.

The Raman spectra were measured between 300 and 10 K in 10 K intervals, shown in Fig. S3. In order to maximize the signal-to-noise ratio and track all phonon modes simultaneously, the temperature dependent measurements were done without the analyzing polarizer. The phonon energies and full-width at half maxima (FWHM) were extracted by fitting to Lorentzian line shapes, such as shown in Fig. S4 for spectra collected at 10 K and 300 K.

In most materials, the phonons could acquire finite line-width through 3 channels, i.e., impurity scattering

(γ_0), anharmonic phonon-phonon interaction ($\gamma_{3p}(T)$), and electron-phonon coupling ($\gamma_{ep}(T)$) [87, 88].

$$\gamma(T) = \gamma_0 + \gamma_{3p}[1 + n(\omega_1, T) + n(\omega_0 - \omega_1, T)] + \gamma_{ep}[f(\omega_a - \omega_0/2) - f(\omega_a + \omega_0/2)] \quad (9)$$

The temperature dependence of FWHM in most materials is dominated by the anharmonic “3-phonon process”, i.e. second term in Eq. 9, where a $q = 0$ optical phonon of ω_0 decays into 2 phonons with opposite momenta and energies ω_1 and $\omega_0 - \omega_1$, and $n(\omega, T) = 1/(\exp(\hbar\omega/k_B T) - 1)$ is the Bose distribution function. The strength of the anharmonicity is determined by $\gamma_{3p} = \frac{18\pi}{\hbar^2} \sum_{q, j_1, j_2} |V(j, 0; j_1, q; j_2, -q)|^2$, where $V(j, 0; j_1, q; j_2, -q)$ is the matrix element for the j -th phonon at $q = 0$ decaying into j_1 -th phonon at q and j_2 -th phonon at $-q$. The last term in Eq. 9 accounts for the line width due to excitation of an electron from state (k, i) to (k, j) by absorbing an optical phonon of energy ω_0 (Fig. 9(c)). The constant γ_{ep} is directly related to the electron-phonon coupling constant, $\lambda = \frac{4}{\pi N(0)} \sum_j \gamma_{ep, j} / \omega_{0, j}^2$ with $N(0)$ being the density of state at Fermi energy [88]. $f(\omega, T) = 1/(\exp(\hbar\omega/k_B T) + 1)$ is the Fermi distribution function. The asymmetric coefficient, ω_a is a phenomenological fitting parameter accounting for the fact that the Fermi level may not lie exactly half-way between the electron and hole states, as shown in Fig. 9(c).

We note that the electron-phonon induced line width is typically negligibly small compared to the anharmonic contribution. This is because $q = 0$ phonons generally only promote vertical interband transitions to conserve both energy and momentum, and therefore have very limited phase space to excite electron-hole pairs. Indeed this is the case with the temperature dependence of the 3 highest energy phonons’ FWHM in LaRhGe₃, *e.g.* the data of $A_1^{(3)}$ in Fig. 9(a). However, we found the FWHM of the 4 lowest energy phonons deviates from the prediction of the anharmonic decay model, and could only be well described by adding the electron-phonon interaction term. In particular, the $A_1^{(1)}$ phonon width increases with decreasing temperature, which cannot be explained by the anharmonic model alone even after adding higher order terms (Fig. 9(a)). Similar effects have been observed in graphite and graphene [87, 89], and more recently in WP₂ and NbGe₂ as a signature of the phonon drag effect [10, 13]. Here, the strong SOC and the lack of inversion symmetry generates several spin-split Fermi surfaces closely separated in energy, splitting for our LaRhGe₃ sample in Fig. S1 and Table S3 is consistent with previous report [28], allowing excitation of electron-hole pairs by absorbing $q = 0$ optical phonons. Furthermore, the almost movable nodal lines near the Fermi level as we discussed in Sec. II C could also be favorable for phonon absorption. We compare the electron-phonon coupling estimated from superconductivity data in Sec. II D, $\lambda_{ep} = 0.33$, with the electron-phonon coupling estimated from the T -dependent data for various

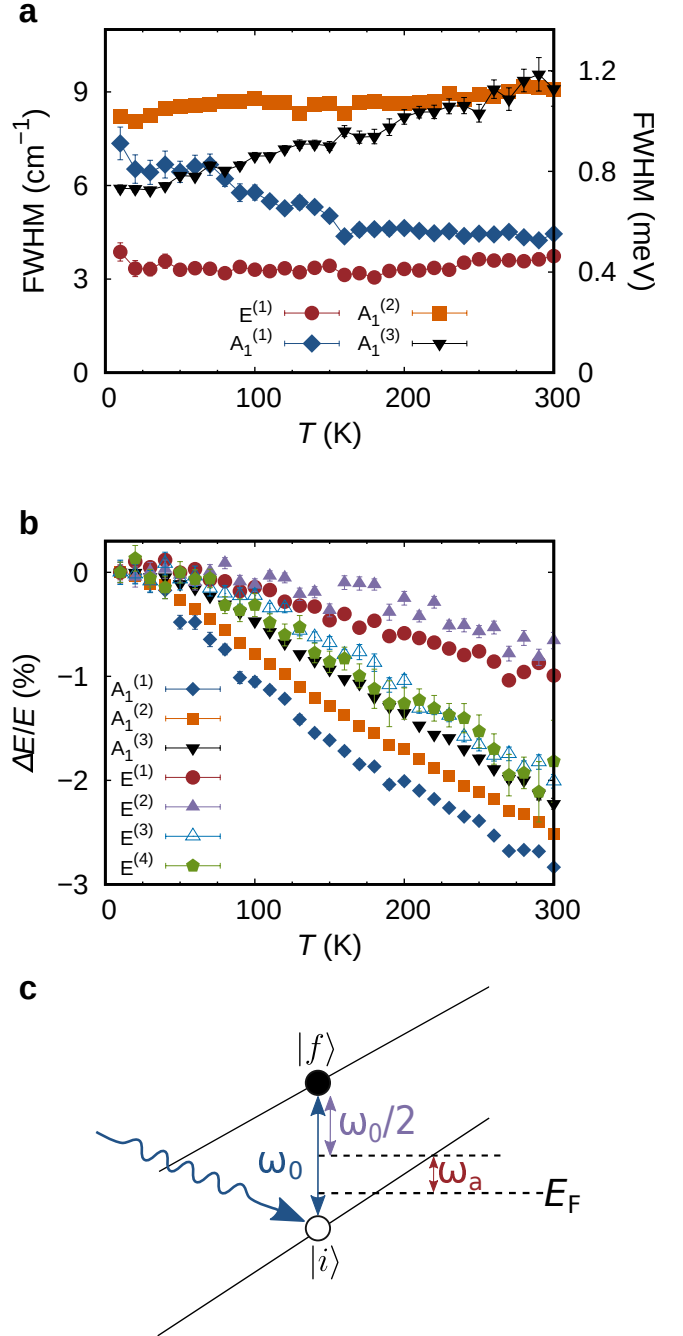


FIG. 9. Anomalous temperature dependence of the $A_1^{(1)}$ phonon lifetime in LaRhGe₃. (a) Full width at half maximum (FWHM) temperature dependence of $A_1^{(1)}$, $A_1^{(2)}$, $A_1^{(3)}$, and $E^{(1)}$ modes based on fits described in the text. (b) Percent difference of the phonon energies of A_1 and E modes from energies at 10 K as a function of temperature. (c) Schematic depicting excitation of electron-hole pairs by optical phonons, where ω_a is the energy offset to take into account that the Fermi level is not exactly halfway between the initial state $|i\rangle$ and final state $|f\rangle$ and ω_0 is the bare phonon energy.

Raman modes in Table S4. We find the total contribution to λ_{ep} from the optical phonons to be around 0.0018,

which is a negligibly small fraction.

Unlike the line width, electron-phonon coupling has little effect on the phonon energy where the temperature dependence is contributed by two major factors, i.e. lattice thermal expansion and anharmonic phonon-phonon interaction [90].

$$\omega(T) = \omega_0 \exp(-3\gamma_G \alpha_0 T) - \omega_{3p}[1 + n(\omega_1, T) + n(\omega_0 - \omega_1, T)] \quad (10)$$

The first term accounts for the lattice thermal expansion, where ω_0 is the bare phonon energy, γ_G is the mode Grüneisen parameter, and α_0 is the temperature independent linear thermal expansion coefficient. The second term arises from the same 3-phonon anharmonic decay process as in Eq. 9. We show the change in relative energy of the A_1 and E modes in Fig. 9(b). All phonon energies decrease monotonically with increasing temperature dominated by the 3-phonon anharmonic term in Eq. 10. In some materials, it is necessary to include higher order anharmonic terms to describe the temperature dependence of phonon self-energy [87, 91]. In LaRhGe₃, we find it only marginally improves the fit for the phonon energies and has little effect on the line width. This gives us confidence that the observed anomalous temperature dependence of phonon line width cannot be caused by higher order anharmonic terms, and is more likely a signature of electron-phonon drag. All of the fitting parameters are tabulated in the Supplemental Material Table S4.

III. SUMMARY

Our study establishes LaRhGe₃ as a remarkable material with many intertwined novel electronic properties. Our transport measurements demonstrate that LaRhGe₃ is a compensated semimetal while our electronic structure calculations reveal Weyl nodal-line states due to the $I4mm$ space group. We report the discovery of superconductivity in LaRhGe₃ with a T_c of 0.39(1) K and a $B_c(0)$ of 2.1(1) mT. We find that LaRhGe₃ is a type-I superconductor and well described by weak-coupling BCS theory with no evidence for TRS breaking in the zero field μ SR measurement suggesting a dominant singlet pairing in the measured temperature range, despite the strong antisymmetric SOC.

In the normal state, we find that the temperature dependence of resistivity in zero-field deviates from that of a typical Fermi liquid. We identify a peak in the derivative of the resistivity, the Seebeck coefficient, and in thermal conductivity at ~ 30 K, which is consistent with electron phonon drag in LaRhGe₃. We measure the Raman spectra of LaRhGe₃ between 10 and 300 K, and find anomalous temperature dependence of phonon line widths that can be explained by assuming electron-phonon coupling. This appears prominent in the temperature dependence of the FWHM of the $A_1^{(1)}$ mode, the lowest energy A_1 mode.

With the rich literature on superconductivity in materials crystallizing in the RTX_3 structure, we draw some comparisons with LaRhGe₃ and find it similar to the previously reported LaRhSi₃. However, our current work indicating semimetallicity and electron-phonon drag in the normal state highlights a new area of interest in the class of non-centrosymmetric materials crystallizing in the $I4mm$ space group. More work is needed to clarify the pairing state in the superconducting phase of LaRhGe₃. Furthermore, the theoretically predicted *almost movable* nodal line will push further investigation of topology, both theoretically and experimentally, in the RTX_3 family of materials.

IV. METHODS

A. Synthesis and Structural Characterization

Single crystals of LaRhGe₃ were grown from Rh-Ge self flux. The elements La, Rh, and Ge in the molar ratio 1:2:7 were loaded into an Al₂O₃ Canfield crucible set and sealed in a quartz tube under 0.3 atm argon pressure. The mixture was then slowly heated to 1200 °C and held at this temperature for 6 h followed by cooling to 975 °C over 60 h. At 975 °C, the crystals were separated from the flux by centrifuging at 2000 rpm for approximately 30 s. The as-grown crystals were shiny with dimensions up to $3 \times 2 \times 1$ mm³, and are stable in air on a time scale of weeks but develop surface oxidation over more extended periods of air exposure. Phase purity and orientation of the crystals were confirmed by X-ray diffraction (XRD) using a Bruker D8 Advance with Cu K α_1 radiation ($\lambda = 1.54056$ Å). The composition and homogeneity were confirmed through energy dispersive X-ray spectroscopy (EDX) using a Philips XL30 scanning electron microscope equipped with a Bruker Quantax 200 energy-dispersion X-ray microanalysis system and an XFlash 6010 SDD detector.

B. Transport and Specific Heat

Electrical resistivity measurements were performed with conventional four- and five-probe geometries using a Quantum Design Physical Property Measurement System (PPMS). For these measurements Pt wires (25 μ m) were attached to the sample with silver epoxy. Specific heat measurements were performed using a PPMS with a ³He/⁴He dilution refrigerator insert. Thermal conductivity and Seebeck measurement were performed using a thermal transport option for the PPMS.

C. μ SR Measurements

Muon spin relaxation measurements were performed using a dilution refrigerator at the M15 beamline at TRI-

UMF. Multiple LaRhGe₃ crystals were mounted on an Ag plate using GE varnish and placed on the sample holder. Careful cancelling of remnant field was performed using a Si semiconductor reference prior to the zero-field experiment. The transverse-field experiment was performed by applying a magnetic field along the plate direction of the sample in spin-rotated mode. Muon analysis was performed in MUSRFIT [92].

D. Raman Measurements

Raman scattering measurements were performed using a Horiba Jobin-Yvon LabRAM monochromator, equipped with 1800 grooves/mm grating and a Peltier cooled CCD camera. The 632.817 nm line of a He-Ne laser was used as the light source, and the spot diameter is about 10 μm on the sample using a 50x microscopic objective for both focusing and collection of light. The spectral resolution is about 1 cm^{-1} in this study. A Semrock RazorEdge filter was used to block the elastically scattered laser light, where the cutoff energy is 79 cm^{-1} . For measured performed at non-ambient temperatures, we used a Cryovac Micro continuous helium flow cryostat, where the sample is thermally anchored to the copper cold-finger and sits in a vacuum environment better than 1×10^{-6} mbar. Measurements were taken at temperatures ranging between 5 to 300 K with 1 K accuracy.

LaRhGe₃ has five atoms in the primitive cell, leading to a total of three acoustic and 12 optical phonon bands. With visible light, Raman scattering only probes a small portion of the Brillouin zone near $q = 0$, where the symmetries of the 12 optical phonons can be denoted by the irreducible representations of the C_{4v} point group: $3A_1 + B_1 + 4E$ [85]. The samples was mounted on the cryostat with the as-grown (101) surface normal to the optical axis. At room temperature, spectra were obtained with the incident and scattered light polarized in the following combinations in order to identify the symmetries

of the studied excitations: $(E_i, E_s) = (x, x)$ couples to phonons with A_1, B_1 and E symmetries, $(E_i, E_s) = (x, y)$ couples only to phonons with the E symmetry. E_i and E_s are the polarizations of the incident and scattered light, respectively. x and y corresponds to $[10\bar{1}]$ and $[010]$ crystal axes, respectively. The analyzing polarizer is removed in temperature dependent experiments to collect data from all phonons in the same cooling cycle.

E. DFT Calculations

Electronic structure calculations were performed within the framework of density functional theory (DFT) as implemented in the VASP package [93–95]. The generalized gradient approximation with the PBE parameterization for the exchange-correlation functional [96, 97] was used. The plane-wave-basis set has been cut off at $E_{\text{cutoff}} = 287.6$ eV and the charge density was converged on a grid of 1792 irreducible k points. The tetragonal crystal structure ($I4mm$, space group no. 107, $a = 4.432$ Å, and $c = 10.101$ Å) was used [28], and structural relaxation resulted in $a = 4.437$ Å, and $c = 10.281$ Å. The phonon modes were computed in a $2 \times 2 \times 1$ conventional supercell using the phonopy package[98, 99].

ACKNOWLEDGMENTS

This research was undertaken thanks in part to funding from the Max Planck-UBC-UTokyo Centre for Quantum Materials and the Canada First Research Excellence Fund, Quantum Materials and Future Technologies Program. This work was also supported by the Natural Sciences and Engineering Research Council of Canada (NSERC), the CIFAR Azrieli Global Scholars program, and the Sloan Research Fellowships program. We thank TRIUMF staff for their technical support during muon experiment. We thank K. Behnia, E. Benckiser, M. Minola, S. Dierker, and M. Sigrist for valuable discussion.

-
- [1] KS Novoselov, AK Geim, SV Morozov, D Jiang, MI Katsonelson, IV Grigorieva, SV Dubonos, and AA Firsov, “Two-dimensional gas of massless Dirac fermions in graphene,” *Nature* **438**, 197–200 (2005).
 - [2] Andre K Geim and Konstantin S Novoselov, “The rise of graphene,” *Nat. Mater.* **6**, 183–191 (2007).
 - [3] AA Burkov, “Topological semimetals,” *Nat. Mater.* **15**, 1145–1148 (2016).
 - [4] Binghai Yan and Claudia Felser, “Topological materials: Weyl semimetals,” *Annu. Rev. Condens. Matter Phys.* **8**, 337–354 (2017).
 - [5] NP Armitage, EJ Mele, and Ashvin Vishwanath, “Weyl and Dirac semimetals in three-dimensional solids,” *Rev. Mod. Phys.* **90**, 015001 (2018).
 - [6] Mazhar N Ali, Jun Xiong, Steven Flynn, Jing Tao, Quinn D Gibson, Leslie M Schoop, Tian Liang, Neel Haldolaarachchige, Max Hirschberger, Nai Phuan Ong, *et al.*, “Large, non-saturating magnetoresistance in WTe₂,” *Nature* **514**, 205–208 (2014).
 - [7] Chandra Shekhar, Ajaya K Nayak, Yan Sun, Marcus Schmidt, Michael Nicklas, Inge Leermakers, Uli Zeitler, Yurii Skourski, Jochen Wosnitza, Zhongkai Liu, *et al.*, “Extremely large magnetoresistance and ultrahigh mobility in the topological Weyl semimetal candidate NbP,” *Nat. Phys.* **11**, 645–649 (2015).
 - [8] Nitesh Kumar, Yan Sun, Nan Xu, Kaustuv Manna, Mengyu Yao, Vicky Süß, Inge Leermakers, Olga Young, Tobias Förster, Marcus Schmidt, *et al.*, “Extremely high magnetoresistance and conductivity

- in the type-II Weyl semimetals WP_2 and MoP_2 ,” *Nat. Commun.* **8**, 1642 (2017).
- [9] M-Y Yao, Nan Xu, QS Wu, Gabriel Autès, Nitesh Kumar, Vladimir N Strocov, Nicholas C Plumb, Milan Radovic, Oleg V Yazyev, Claudia Felser, *et al.*, “Observation of weyl nodes in robust type-II Weyl semimetal WP_2 ,” *Phys. Rev. Lett.* **122**, 176402 (2019).
- [10] Gavin B. Osterhoudt, Yaxian Wang, Christina A. C. Garcia, Vincent M. Plisson, Johannes Gooth, Claudia Felser, Prineha Narang, and Kenneth S. Burch, “Evidence for dominant phonon-electron scattering in Weyl semimetal WP_2 ,” *Phys. Rev. X* **11**, 011017 (2021).
- [11] Yun Wu, Lin-Lin Wang, Eundeok Mun, Duane D Johnson, Daixiang Mou, Lunan Huang, Yongbin Lee, Serguei L Bud’ko, Paul C Canfield, and Adam Kaminski, “Dirac node arcs in $PtSn_4$,” *Nat. Phys.* **12**, 667–671 (2016).
- [12] Chenguang Fu, Satya N Guin, Thomas Scaffidi, Yan Sun, Rana Saha, Sarah J Watzman, Abhay K Srivastava, Guowei Li, Walter Schnelle, Stuart SP Parkin, *et al.*, “Largely suppressed magneto-thermal conductivity and enhanced magneto-thermoelectric properties in $PtSn_4$,” *Research* (2020).
- [13] Hung-Yu Yang, Xiaohan Yao, Vincent Plisson, Shirin Mozaffari, Jan P Scheifers, Aikaterini Flessa Savvidou, Eun Sang Choi, Gregory T McCandless, Mathieu F Padlewski, Carsten Putzke, Philip J. W. Moll, Julia Y. Chan, Luis Balicas, Kenneth S. Burch, and Fazel Tafti, “Evidence of a coupled electron-phonon liquid in $NbGe_2$,” *Nat. Commun.* **12**, 5292 (2021).
- [14] Eve Emmanouilidou, Sougata Mardanya, Jie Xing, PV Sreenivasa Reddy, Amit Agarwal, Tay-Rong Chang, and Ni Ni, “Fermiology and type-I superconductivity in the chiral superconductor $NbGe_2$ with Kramers-Weyl fermions,” *Phys. Rev. B* **102**, 235144 (2020).
- [15] E. Bauer, G. Hilscher, H. Michor, Ch. Paul, E. W. Scheidt, A. Griбанov, Yu. Seropugin, H. Noël, M. Sigrist, and P. Rogl, “Heavy fermion superconductivity and magnetic order in noncentrosymmetric $CePt_3Si$,” *Phys. Rev. Lett.* **92**, 027003 (2004).
- [16] E. Bauer and M. Sigrist, *Non-Centrosymmetric Superconductors: Introduction and Overview* (Berlin: Springer, 2012).
- [17] M Smidman, M B Salamon, H Q Yuan, and D F Agterberg, “Superconductivity and spin-orbit coupling in non-centrosymmetric materials: a review,” *Rep. Prog. Phys.* **80**, 036501 (2017).
- [18] Sungkit Yip, “Noncentrosymmetric superconductors,” *Annu. Rev. Condens. Matter Phys.* **5**, 15–33 (2014).
- [19] Andreas P Schnyder and Philip M R Brydon, “Topological surface states in nodal superconductors,” *J. Phys. Condens. Matter* **27**, 243201 (2015).
- [20] Matthias Bode, M Heide, K Von Bergmann, P Ferriani, Stefan Heinze, G Bihlmayer, A Kubetzka, O Pietzsch, Stefan Blügel, and R Wiesendanger, “Chiral magnetic order at surfaces driven by inversion asymmetry,” *nature* **447**, 190–193 (2007).
- [21] Naoto Nagaosa and Yoshinori Tokura, “Topological properties and dynamics of magnetic skyrmions,” *Nature nanotechnology* **8**, 899–911 (2013).
- [22] N Kimura, K Ito, K Saitoh, Y Umeda, H Aoki, and T Terashima, “Pressure-induced superconductivity in noncentrosymmetric heavy-fermion $CeRhSi_3$,” *Phys. Rev. Lett.* **95**, 247004 (2005).
- [23] Ichiro Sugitani, Yusuke Okuda, Hiroaki Shishido, Tsutomu Yamada, Arumugam Thamizhavel, Etsuji Yamamoto, Tatsuma D Matsuda, Yoshinori Haga, Tetsuya Takeuchi, Rikio Settai, *et al.*, “Pressure-induced heavy-fermion superconductivity in antiferromagnet $CeIrSi_3$ without inversion symmetry,” *J. Phys. Soc. Jpn.* **75**, 043703–043703 (2006).
- [24] Yusuke Okuda, Yuichiro Miyauchi, Yuki Ida, Yuuji Takeda, Chie Tonohiro, Yasuhiro Oduchi, Tsutomu Yamada, Nguyen Duc Dung, Tatsuma D. Matsuda, Yoshinori Haga, *et al.*, “Magnetic and superconducting properties of $LaIrSi_3$ and $CeIrSi_3$ with the non-centrosymmetric crystal structure,” *J. Phys. Soc. Jpn.* **76**, 044708 (2007).
- [25] Noriaki Kimura, Yuji Muro, and Haruyoshi Aoki, “Normal and superconducting properties of noncentrosymmetric heavy fermion $CeRhSi_3$,” *J. Phys. Soc. Jpn.* **76**, 051010–051010 (2007).
- [26] Rikio Settai, Tetsuya Takeuchi, and Yoshichika Ōnuki, “Recent advances in Ce-based heavy-fermion superconductivity and Fermi surface properties,” *J. Phys. Soc. Jpn.* **76**, 051003 (2007).
- [27] Marie-aude Méasson, Hiroshi Muranaka, Tomoya Kawai, Yuuki Ota, Kiyohiro Sugiyama, Masayuki Hagiwara, Koichi Kindo, Tetsuya Takeuchi, Katsuya Shimizu, Fuminori Honda, *et al.*, “Magnetic properties of $RCoGe_3$ (R : Ce, Pr, and Nd) and strong anisotropy of the upper critical field in non-centrosymmetric compound $CeCoGe_3$,” *J. Phys. Soc. Jpn.* **78**, 124713 (2009).
- [28] Tomoya Kawai, Hiroshi Muranaka, Toyooki Endo, Nguyen Duc Dung, Yusuke Doi, Shugo Ikeda, Tatsuma D Matsuda, Yoshinori Haga, Hisatomo Harima, Rikio Settai, and Yoshichika Onuki, “Split Fermi surface properties of $LaTGe_3$ (T: transition metal) and $PrCoGe_3$ with the non-centrosymmetric crystal structure,” *J. Phys. Soc. Jpn.* **77**, 064717–064717 (2008).
- [29] G Eguchi, DC Peets, M Kriener, Y Maeno, E Nishibori, Y Kumazawa, K Banno, S Maki, and H Sawa, “Crystallographic and superconducting properties of the fully gapped noncentrosymmetric 5d-electron superconductors $CaMSi_3$ ($M = Ir, Pt$),” *Phys. Rev. B* **83**, 024512 (2011).
- [30] Masaaki Isobe, Hiroyuki Yoshida, Koji Kimoto, Masao Arai, and Eiji Takayama-Muromachi, “ $SrAuSi_3$: A noncentrosymmetric superconductor,” *Chemistry of Materials* **26**, 2155–2165 (2014).
- [31] G Venturini, M Méot-Meyer, B Malaman, and B Roques, “De nouvelles séries de germaniures, isotopes de $Yb_3Rh_4Sn_{13}$ et $BaNiSn_3$, dans les systèmes ternaires TR–T–Ge où TR est un élément des terres rares et $T \equiv Co, Rh, Ir, Ru, Os$,” *J. Less-Common Met.* **113**, 197–204 (1985).
- [32] Alfred Brian Pippard, *Magnetoresistance in metals*, Vol. 2 (Cambridge university press, 1989).
- [33] Yi-Yan Wang, Qiao-He Yu, Peng-Jie Guo, Kai Liu, and Tian-Long Xia, “Resistivity plateau and extremely large magnetoresistance in $NbAs_2$ and $TaAs_2$,” *Phys. Rev. B* **94**, 041103 (2016).
- [34] Aifeng Wang, D Graf, Yu Liu, Qianheng Du, Jiabao Zheng, Hechang Lei, and C Petrovic, “Large magnetoresistance in the type-II Weyl semimetal WP_2 ,” *Phys. Rev. B* **96**, 121107 (2017).
- [35] J Bannies, E Razzoli, M Michiardi, H-H Kung, IS Elfimov, M Yao, A Fedorov, J Fink, C Jozwiak, A Bostwick, *et al.*, “Extremely large magnetoresistance from electron-hole compensation in the nodal-loop semimetal ZrP_2 ,”

- Phys. Rev. B* **103**, 155144 (2021).
- [36] Moritz M Hirschmann, Andreas Leonhardt, Berkay Kilic, Douglas H Fabini, and Andreas P Schnyder, “Symmetry-enforced band crossings in tetragonal materials: Dirac and Weyl degeneracies on points, lines, and planes,” *Phys. Rev. Mater.* **5**, 054202 (2021).
- [37] Hongming Weng, Yunye Liang, Qiunan Xu, Rui Yu, Zhong Fang, Xi Dai, and Yoshiyuki Kawazoe, “Topological node-line semimetal in three-dimensional graphene networks,” *Phys. Rev. B* **92**, 045108 (2015).
- [38] Y.-H. Chan, Ching-Kai Chiu, M. Y. Chou, and Andreas P. Schnyder, “ Ca_3P_2 and other topological semimetals with line nodes and drumhead surface states,” *Phys. Rev. B* **93**, 205132 (2016).
- [39] C. K. Chiu, Y. H. Chan, and A. P. Schnyder, “Quantized berry phase and surface states under reflection symmetry or space-time inversion symmetry,” *arXiv preprint arXiv:1810.04094* (2018).
- [40] Pengzi Liu, James R Williams, and Judy J Cha, “Topological nanomaterials,” *Nat. Rev. Mater.* **4**, 479–496 (2019).
- [41] Jifa Tian, Ireneusz Miotkowski, Seokmin Hong, and Yong P Chen, “Electrical injection and detection of spin-polarized currents in topological insulator $\text{Bi}_2\text{Te}_2\text{Se}$,” *Sci. Rep.* **5**, 14293 (2015).
- [42] Jifa Tian, Seokmin Hong, Ireneusz Miotkowski, Supriyo Datta, and Yong P Chen, “Observation of current-induced, long-lived persistent spin polarization in a topological insulator: A rechargeable spin battery,” *Sci. Adv.* **3**, e1602531 (2017).
- [43] Peng Li, Weikang Wu, Yan Wen, Chenhui Zhang, Junwei Zhang, Senfu Zhang, Zhiming Yu, Shengyuan A Yang, Aurelien Manchon, and Xi-xiang Zhang, “Spin-momentum locking and spin-orbit torques in magnetic nano-heterojunctions composed of Weyl semimetal WTe_2 ,” *Nat. Commun.* **9**, 3990 (2018).
- [44] Jimin Kim, Seung Su Baik, Sae Hee Ryu, Yeongsup Sohn, Soohyung Park, Byeong-Gyu Park, Jonathan Denlinger, Yeonjin Yi, Hyoung Joon Choi, and Keun Su Kim, “Observation of tunable band gap and anisotropic Dirac semimetal state in black phosphorus,” *Science* **349**, 723–726 (2015).
- [45] Rex Lundgren, Pontus Laurell, and Gregory A Fiete, “Thermoelectric properties of Weyl and Dirac semimetals,” *Phys. Rev. B* **90**, 165115 (2014).
- [46] Qingsheng Wang, Cai-Zhen Li, Shaofeng Ge, Jin-Guang Li, Wei Lu, Jiawei Lai, Xuefeng Liu, Junchao Ma, Da-Peng Yu, Zhi-Min Liao, *et al.*, “Ultrafast broadband photodetectors based on three-dimensional Dirac semimetal Cd_3As_2 ,” *Nano letters* **17**, 834–841 (2017).
- [47] Chunyu Guo, Lunhui Hu, Carsten Putzke, Jonas Diaz, Xiangwei Huang, Kaustuv Manna, Feng-Ren Fan, Chandra Shekhar, Yan Sun, Claudia Felser, Chaoping Liu, B. Andrei Bernevig, and Philip J. W. Moll, “Quasi-symmetry-protected topology in a semi-metal,” *Nature Physics* **18**, 813–818 (2022).
- [48] Chao Shang, Owen Ganter, Niclas Heinsdorf, and Stephen M. Winter, “irf₄: From tetrahedral compass model to topological semimetal,” *Phys. Rev. B* **107**, 125111 (2023).
- [49] V. Gurarie, “Single-particle green’s functions and interacting topological insulators,” *Phys. Rev. B* **83**, 085426 (2011).
- [50] Zhong Wang and Shou-Cheng Zhang, “Simplified topological invariants for interacting insulators,” *Phys. Rev. X* **2**, 031008 (2012).
- [51] Xue-Yang Song and Andreas P. Schnyder, “Interaction effects on the classification of crystalline topological insulators and superconductors,” *Phys. Rev. B* **95**, 195108 (2017).
- [52] Mikel Iraola, Niclas Heinsdorf, Apoorv Tiwari, Dominik Lessnich, Thomas Mertz, Francesco Ferrari, Mark H. Fischer, Stephen M. Winter, Frank Pollmann, Titus Neupert, Roser Valentí, and Maia G. Vergniory, “Towards a topological quantum chemistry description of correlated systems: The case of the hubbard diamond chain,” *Phys. Rev. B* **104**, 195125 (2021).
- [53] Rajesh Chaunsali, Haitao Xu, Jinkyu Yang, Panayotis G. Kevrekidis, and Georgios Theocharis, “Stability of topological edge states under strong nonlinear effects,” *Phys. Rev. B* **103**, 024106 (2021).
- [54] Yuxuan Wang and Rahul M. Nandkishore, “Topological surface superconductivity in doped weyl loop materials,” *Phys. Rev. B* **95**, 060506 (2017).
- [55] WL McMillan, “Transition temperature of strong-coupled superconductors,” *Phys. Rev.* **167**, 331 (1968).
- [56] YJ Uemura, “Condensation, excitation, pairing, and superfluid density in high- t_c superconductors: the magnetic resonance mode as a roton analogue and a possible spin-mediated pairing,” *J. Condens. Matter Phys.* **16**, S4515 (2004).
- [57] PP Poole, HA Farach, RJ Creswick, and R Prozorov, “Superconductivity,” (2007).
- [58] JP Carbotte, “Properties of boson-exchange superconductors,” *Rev. Mod. Phys.* **62**, 1027 (1990).
- [59] Gerald E Peabody and R Meservey, “Magnetic flux penetration into superconducting thin films,” *Phys. Rev. B* **6**, 2579 (1972).
- [60] Devashibhai T Adroja, Franziska KK Kirschner, Franz Lang, Michael Smidman, Adrian D Hillier, Zhi-Cheng Wang, Guang-Han Cao, Gavin BG Stenning, and Stephen J Blundell, “Multigap superconductivity in $\text{RbCa}_2\text{Fe}_4\text{As}_4\text{F}_2$ investigated using μSR measurements,” *J. Phys. Soc. Japan* **87**, 124705 (2018).
- [61] Mohammed A Albedah, Farshad Nejadshattari, Zbigniew M Stadnik, Zhi-Cheng Wang, Cao Wang, and Guang-Han Cao, “Absence of the stripe antiferromagnetic order in the new 30 k superconductor ThFeAsN ,” *J. Alloys Compd.* **695**, 1128–1136 (2017).
- [62] A Bhattacharyya, DT Adroja, M Smidman, and VK Anand, “A brief review on μSR studies of unconventional Fe- and Cr-based superconductors,” *Sci. China: Phys. Mech. Astron.* **61**, 1–22 (2018).
- [63] JE Sonier, SA Sabok-Sayr, FD Callaghan, CV Kaiser, V Pacradouni, JH Brewer, SL Stubbs, WN Hardy, DA Bonn, Ruixing Liang, and W. A. Atkinson, “Hole-doping dependence of the magnetic penetration depth and vortex core size in $\text{YBa}_2\text{Cu}_3\text{O}_y$: Evidence for stripe correlations near 1/8 hole doping,” *Phys. Rev. B* **76**, 134518 (2007).
- [64] YJ Uemura, “Muon spin relaxation studies on high- t_c , organic, heavy-fermion, and Chevrel phase superconductors,” *Phys. B: Condens. Matter* **169**, 99–106 (1991).
- [65] Evgeny F Talantsev and Jeffery L Tallon, “Universal self-field critical current for thin-film superconductors,” *Nat. Commun.* **6**, 7820 (2015).

- [66] YJ Uemura, GM Luke, BJ Sternlieb, JH Brewer, JF Carolan, WN Hardy, R Kadono, JR Kempton, RF Kiefl, SR Kreitzman, *et al.*, “Universal correlations between t_c and n_s/m^* (carrier density over effective mass) in high- t_c cuprate superconductors,” *Phys. Rev. Lett.* **62**, 2317 (1989).
- [67] Xiao Lin, Zengwei Zhu, Benoît Fauqué, and Kamran Behnia, “Fermi surface of the most dilute superconductor,” *Phys. Rev. X* **3**, 021002 (2013).
- [68] Ernst Bauer, RT Khan, Herwig Michor, Esmail Royanian, A Grytsiv, N Melnychenko-Koblyuk, P Rogl, D Reith, R Podloucky, E-W Scheidt, *et al.*, “BaPtSi₃: A noncentrosymmetric BCS-like superconductor,” *Phys. Rev. B* **80**, 064504 (2009).
- [69] F Kneidinger, L Salamakha, E Bauer, I Zeiringer, P Rogl, C Blaas-Schneider, D Reith, and R Podloucky, “Superconductivity in noncentrosymmetric BaAl₄ derived structures,” *Phys. Rev. B* **90**, 024504 (2014).
- [70] VK Anand, AD Hillier, DT Adroja, AM Strydom, H Michor, KA McEwen, and BD Rainford, “Specific heat and μ SR study on the noncentrosymmetric superconductor LaRhSi₃,” *Phys. Rev. B* **83**, 064522 (2011).
- [71] Jiro Kitagawa, Yuji Muro, Naoya Takeda, and Masayasu Ishikawa, “Low-temperature magnetic properties of several compounds in Ce–Pd–x (x = Si, Ge and Al) ternary systems,” *J. Phys. Soc. Jpn.* **66**, 2163–2174 (1997).
- [72] M Smidman, AD Hillier, DT Adroja, MR Lees, V Kn Anand, Ravi P Singh, RI Smith, DM Paul, and G Balakrishnan, “Investigations of the superconducting states of noncentrosymmetric LaPdSi₃ and LaPtSi₃,” *Phys. Rev. B* **89**, 094509 (2014).
- [73] V Kn Anand, D Britz, A Bhattacharyya, DT Adroja, AD Hillier, AM Strydom, W Kockelmann, BD Rainford, and Kn A McEwen, “Physical properties of noncentrosymmetric superconductor LaIrSi₃: A μ SR study,” *Phys. Rev. B* **90**, 014513 (2014).
- [74] Ravi P Singh, AD Hillier, D Chowdhury, JAT Barker, D McK Paul, MR Lees, and G Balakrishnan, “Probing the superconducting ground state of the noncentrosymmetric superconductors CaT₂Si₃ (T = Ir, Pt) using muon-spin relaxation and rotation,” *Phys. Rev. B* **90**, 104504 (2014).
- [75] Kn Miliyanchuk, Friedrich Kneidinger, C Blaas-Schneider, D Reith, R Podloucky, P Rogl, T Khan, L Salamakha, G Hilscher, H Michor, *et al.*, “Platinum metal silicides and germanides: superconductivity in noncentrosymmetric intermetallics,” in *J. Phys. Conf. Ser.*, Vol. 273 (IOP Publishing, 2011) p. 012078.
- [76] GW Hull, JH Wernick, TH Geballe, JV Waszczak, and JE Bernardini, “Superconductivity in the ternary intermetallics YbPd₂Ge₂, LaPd₂Ge₂, and LaPt₂Ge₂,” *Phys. Rev. B* **24**, 6715 (1981).
- [77] TTM Palstra, G Lu, AA Menovsky, GJ Nieuwenhuys, PH Kes, and JA Mydosh, “Superconductivity in the ternary rare-earth (Y, La, and Lu) compounds RPD₂Si₂ and RRh₂Si₂,” *Phys. Rev. B* **34**, 4566 (1986).
- [78] Shingo Yonezawa and Yoshiteru Maeno, “Type-I superconductivity of the layered silver oxide Ag₅Pb₂O₆,” *Phys. Rev. B* **72**, 180504 (2005).
- [79] Carolina A Marques, Matthew James Neat, Chi Ming Yim, Matthew David Watson, Luke Charles Rhodes, Christoph Heil, KS Pervakov, VA Vlasenko, VM Pudalov, AV Muratov, *et al.*, “Electronic structure and superconductivity of the non-centrosymmetric Sn₄As₃,” *New J. Phys.* **22**, 063049 (2020).
- [80] T Terashima, M Kimata, S Uji, T Sugawara, N Kimura, Hayuyoshi Aoki, H Harima, *et al.*, “Fermi surface in LaRhSi₃ and CeRhSi₃,” *Phys. Rev. B* **78**, 205107 (2008).
- [81] JF Kos, “Evidence of phonon drag in the electrical resistivity of silver,” *Phys. Status Solidi B* **52**, 389–394 (1972).
- [82] Alexandre Jaoui, Adrien Gourgout, Gabriel Seyfarth, Alaska Subedi, Thomas Lorenz, Benoît Fauqué, and Kamran Behnia, “Formation of an electron-phonon bifluid in bulk antimony,” *Phys. Rev. X* **12**, 031023 (2022).
- [83] Yu. S. Ponomov and S. V. Streltsov, “Raman-active E_{2g} phonon in MgB₂: Electron-phonon interaction and anharmonicity,” *Phys. Rev. B* **96**, 214503 (2017).
- [84] Nina Girotto and Dino Novko, “Dynamical renormalization of electron-phonon coupling in conventional superconductors,” *Phys. Rev. B* **107**, 064310 (2023).
- [85] E. Kroumova, M.I. Aroyo, J.M. Perez-Mato, A. Kirov, C. Capillas, S. Ivantchev, and H. Wondratschek, “Bilbao crystallographic server : Useful databases and tools for phase-transition studies,” *Phase Transitions* **76**, 155–170 (2003).
- [86] William Hayes and Rodney Loudon, *Scattering of light by crystals* (Wiley, 1978).
- [87] Nicola Bonini, Michele Lazzeri, Nicola Marzari, and Francesco Mauri, “Phonon anharmonicities in graphite and graphene,” *Phys. Rev. Lett.* **99**, 176802 (2007).
- [88] Philip B. Allen and Richard Silbergliitt, “Some effects of phonon dynamics on electron lifetime, mass renormalization, and superconducting transition temperature,” *Phys. Rev. B* **9**, 4733–4741 (1974).
- [89] H-N Liu, X Cong, M-L Lin, and P-H Tan, “The intrinsic temperature-dependent Raman spectra of graphite in the temperature range from 4K to 1000K,” *Carbon* **152**, 451–458 (2019).
- [90] José Menéndez and Manuel Cardona, “Temperature dependence of the first-order Raman scattering by phonons in Si, Ge, and α –Sn: Anharmonic effects,” *Phys. Rev. B* **29**, 2051–2059 (1984).
- [91] Mai Ye, H.-H. Kung, Priscila F. S. Rosa, Eric D. Bauer, Zachary Fisk, and Girsh Blumberg, “Raman spectroscopy of f -electron metals: An example of CeB₆,” *Phys. Rev. Mater.* **3**, 065003 (2019).
- [92] A Suter and BM Wojek, “MUSRFIT: a free platform-independent framework for μ SR data analysis,” *Physics Procedia* **30**, 69–73 (2012).
- [93] G. Kresse and J. Hafner, “Ab initio molecular dynamics for liquid metals,” *Phys. Rev. B* **47**, 558–561 (1993).
- [94] Georg Kresse and Jürgen Furthmüller, “Efficiency of ab-initio total energy calculations for metals and semiconductors using a plane-wave basis set,” *Comput. Mater. Sci.* **6**, 15–50 (1996).
- [95] G. Kresse and J. Furthmüller, “Efficient iterative schemes for ab initio total-energy calculations using a plane-wave basis set,” *Phys. Rev. B* **54**, 11169–11186 (1996).
- [96] John P Perdew, Kieron Burke, and Yue Wang, “Generalized gradient approximation for the exchange-correlation hole of a many-electron system,” *Phys. Rev. B* **54**, 16533 (1996).
- [97] John P. Perdew, Kieron Burke, and Matthias Ernzerhof, “Generalized gradient approximation made simple,”

Phys. Rev. Lett. **77**, 3865–3868 (1996).

[98] A Togo and I Tanaka, “First principles phonon calculations in materials science,” *Scr. Mater.* **108**, 1–5 (2015).

[99] Atsushi Togo, “First-principles phonon calculations with Phonopy and Phono3py,” *J. Phys. Soc. Jpn.* **92**, 012001 (2023).

Supplemental Materials:
Discovery of Superconductivity and Electron-Phonon Drag in
the Non-Centrosymmetric Semimetal LaRhGe₃

TABLE S1. LaRhGe₃ crystals structure refinement fit results.

| Parameter | Value |
|------------------------------------|------------------------------------------------|
| Chemical Formula | LaRhGe ₃ |
| Formula weight | 459.73 |
| Temperature (K) | 300 |
| Crystal System | Tetragonal |
| Space Group | <i>I4mm</i> |
| <i>a</i> , (Å) | 4.4187(2) |
| <i>c</i> , (Å) | 10.0494(5) |
| Volume (Å ³) | 196.21(6) |
| Z | 2 |
| ρ_{calc} (g/cm ³) | 7.781 |
| Radiation | Cu _{kα1} = 1.5406 Å |
| <i>R</i> _{Bragg} | 1.544 |

TABLE S2. Refined atomic positions of LaRhGe₃.

| Atom | <i>x</i> | <i>y</i> | <i>z</i> |
|------|----------|----------|----------|
| La | 0.0 | 0.0 | 0.0 |
| Rh | 0.0 | 0.0 | 0.65762 |
| Ge1 | 0.0 | 0.0 | 0.42106 |
| Ge2 | 0.0 | 0.5 | 0.25990 |

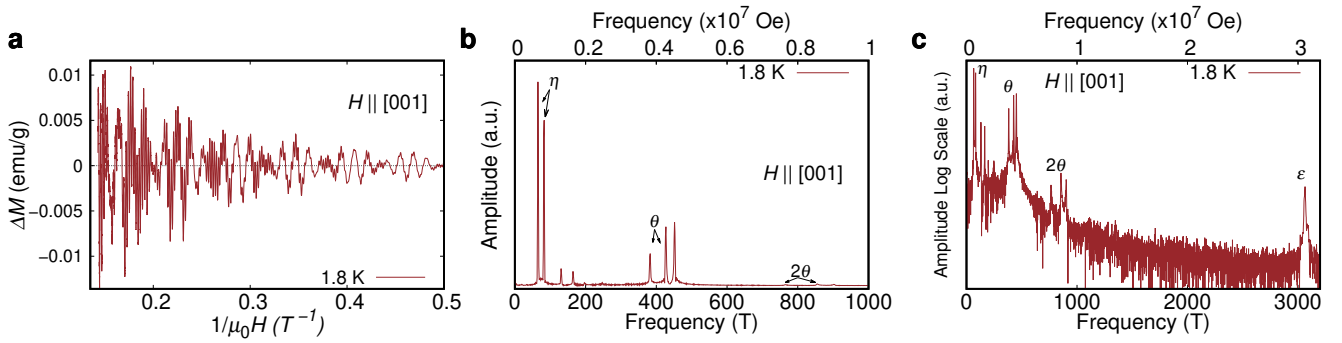


FIG. S1. (a) Oscillatory component ΔM corresponding to the de Haas-van Alphen (dHvA) oscillations in LaRhGe₃ measured at 1.8 K. (b) Fast Fourier Transform spectrum of the dHvA oscillations in (a).

TABLE S3. Comparing de Haas-van Alphen (dHvA) oscillations Frequency in our LaRhGe₃ samples with Literature [S28].

| Branch | $F (\times 10^7 \text{ Oe})$ | $F_{\text{literature}} (\times 10^7 \text{ Oe})$ [S28] |
|------------------|------------------------------|--------------------------------------------------------|
| ϵ (1st) | 3.09 | 3.06 |
| ϵ (2nd) | 3.06 | 3.04 |
| θ (1st) | 0.43 | 0.44 |
| θ (2nd) | 0.38 | 0.38 |
| η (1st) | 0.082 | 0.08 |
| η (2nd) | 0.065 | 0.06 |

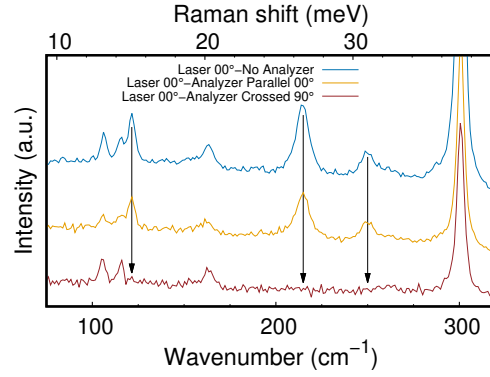


FIG. S2. Raman spectra collected with fixed linearly polarized laser, and polarization analyzer at different orientations. The blue curve shows data without the analyzer (mixed parallel and perpendicular); orange curve is the analyzer polarization parallel to the laser (xx geometry); red curve is the analyzer 90° rotated with respect to laser polarization (xy geometry). Three phonon modes that are strongly suppressed were highlighted with arrows, demonstrating that these are A_1 modes of LaRhGe₃.

TABLE S4. Calculated energies and symmetries of the phonon modes for LaRhGe₃ and comparison with the fitting parameters of Eq. 10 based on our Raman spectra in Fig. S3. All units are in cm⁻¹. The errors represent one standard deviation of the least-squared fit.

| DFT | $\omega(10 \text{ K})$ | ω_0 | ω_1 | ω_{3p} | γ_0 | γ_{3p} | γ_{ep} | ω_a |
|-------------------|------------------------|------------|--------------|---------------|------------|---------------|---------------|------------|
| $E^{(1)}$ 98.1 | 107.0(1) | 107.3(1) | $\omega_0/2$ | 0.18(8) | 1.8(4) | 0.27(6) | 2.3(7) | 47(4) |
| $E^{(2)}$ 108.6 | 116.3(1) | 116.6(1) | $\omega_0/2$ | 0.14(19) | 1.6(5) | 0.36(8) | 2.0(9) | 39(19) |
| $A_1^{(1)}$ 112.8 | 124.9(1) | 125.2(1) | $\omega_0/2$ | 0.60(2) | 0.9(8) | 0.59(14) | 9.9(15) | 61(1) |
| $B_1^{(1)}$ 159.1 | 141.6(6) | 142.6(4) | $\omega_0/2$ | 0.50(60) | 0(17) | 1.0(30) | 24(29) | 71(5) |
| $E^{(3)}$ 162.0 | 166.2(2) | 167.2(1) | $\omega_0/2$ | 0.86(2) | 3(10) | 0.7(18) | 2.1(77) | -14(645) |
| $A_1^{(2)}$ 207.9 | 219.9(0) | 221.1(1) | $\omega_0/2$ | 1.85(5) | 8.2(1) | 0.22(3) | — | — |
| $A_1^{(3)}$ 240.8 | 255.2(0) | 256.6(4) | 52(6) | 1.4(4) | 5.1(1) | 0.84(4) | — | — |
| $E^{(4)}$ 252.7 | 267.1(3) | 268.8(15) | 61(22) | 1.6(15) | 1.4(9) | 2.4(3) | — | — |

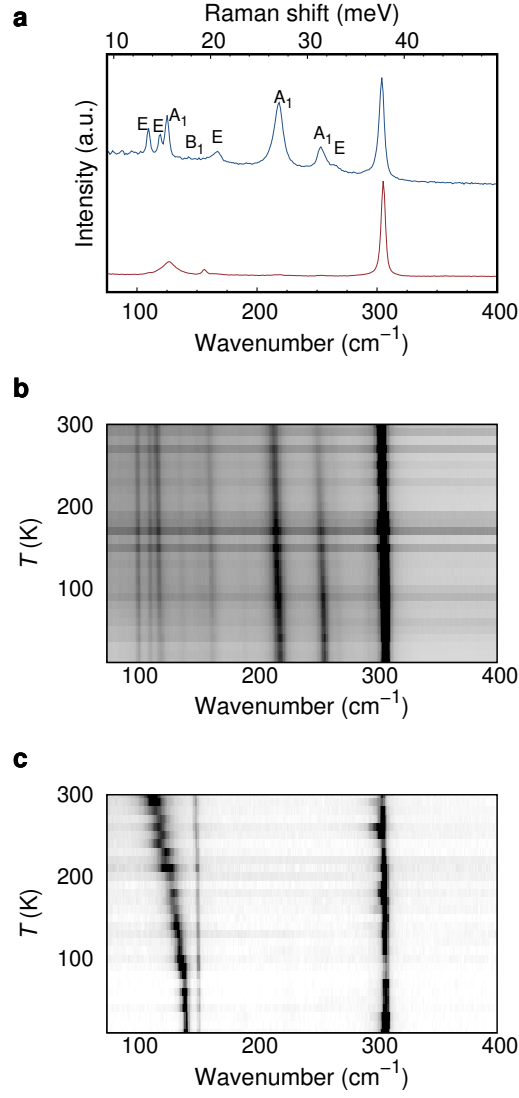


FIG. S3. (a) Raman spectra of LaRhGe₃ measured along different directions of the crystal at room temperature. (b) Black and white map of Raman scattering intensity plotted as a function of temperature and Raman shift measured from the (101) surface of LaRhGe₃ crystal. Unless otherwise specified, all of the Raman data in this work were taken from this sample. (c) Black and white map of Raman scattering intensity measured from the same sample as panel (b), but from a different spot. Since this data was not reproduced by other crystals that we measured, this spot is likely a crystallite with different orientation and possibly even different stoichiometry as the host crystal. However, we highlight the mode at 144 cm⁻¹ at 10 K where the energy softens drastically with increasing temperature, to 120 cm⁻¹ at 300 K. Such large temperature dependence is highly unusual and is difficult to reconcile with the moderate anharmonicity found in LaRhGe₃. The energy of this mode is in the vicinity of the the $A_1^{(1)}$ mode that shows strong electron-phonon coupling, raising the possibility of electron-phonon induced self-energy effect. However, more study is required on this crystallite before any conclusion can be drawn. In this paper, our discussion is focused on data in panel (b) which is reproduced across samples.

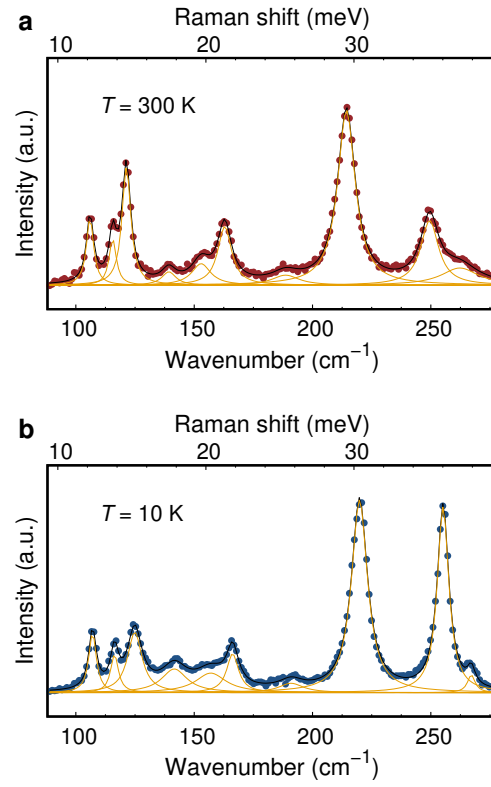


FIG. S4. Raman spectra of LaRhGe_3 measured at 300 K (a) and 10 K (b), sliced from Fig. S3(b) to showcase the extraction of phonon energy and width through fitting. Measured data shown as points and fitted curves for each phonon mode shown individually in yellow and total fit in black.

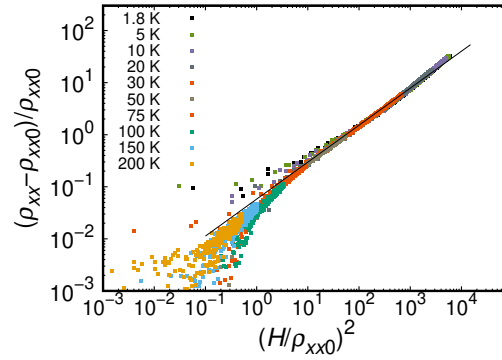


FIG. S5. Kohler scaling analysis of MR data shown in main text (Fig. 7). Any change of slope related to the electron phonon drag in the current data is unclear.

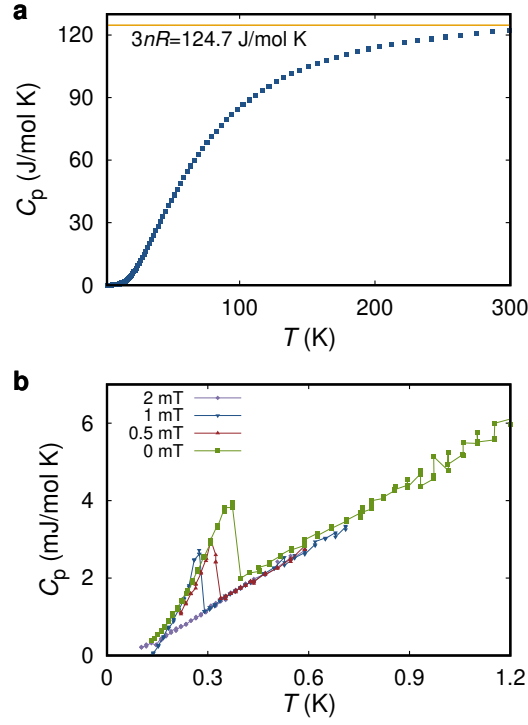


FIG. S6. (a) Temperature dependence of C_P measured between 2-300 K, which shows that the high temperature region approaches the Dulong-Petit limit. (b) Temperature dependence of C_P measured in different applied magnetic fields, showing the superconducting transition, $T_c 0.39(1)$ K in zero-field, that gets suppressed with applied field. Fit to the data above T_c to the form γ and β taking into account the electronic and the phononic contributions. The phononic contribution was subtracted to obtain the C_{el} in the main text.